Role of inclusion stiffness and interfacial strength on dynamic matrix crack growth: An experimental study

Kailash C. Jajam, Hareesh V. Tippur *

Department of Mechanical Engineering, Auburn University, Auburn, AL 36849, USA

ABSTRACT

Experimental simulations of dynamic crack growth past inclusions of two different elastic moduli, stiff (glass) and compliant (polyurethane) relative to the matrix (epoxy), are carried out in a 2D setting. Full-field surface deformations are mapped in the crack–inclusion vicinity optically. The crack growth behavior as a function of inclusion–matrix interfacial strength and the inclusion location relative to the crack is studied under stress-wave loading conditions. An ultra high-speed rotating mirror-type digital camera is used to record random speckle patterns in the crack–inclusion vicinity to quantify in-plane displacement fields. The crack-tip deformation histories from the time of impact until complete fracture are mapped and fracture parameters are extracted. The crack front is arrested by the symmetrically located compliant inclusion for about half the duration needed for complete fracture event. The dynamically propagating crack is attracted and trapped by the weakly bonded inclusion interface for both stiff and compliant symmetrically located inclusion cases, whereas it is deflected away by the strongly bonded stiff inclusion and attracted by strongly bonded compliant inclusion when located eccentrically. The crack is arrested by a strongly bonded compliant inclusion for a significant fraction of the total dynamic event and is longer than the one for the weakly bonded counterpart. The compliant inclusion cases show higher fracture toughness than the stiff inclusion cases. Measured crack-tip mode-mixities correlate well with the observed crack attraction and repulsion mechanisms. Macroscopic examination of fracture surfaces reveals much higher surface roughness and ruggedness after crack–inclusion interaction for compliant inclusion than the stiff one. Implications of these observations on the dynamic fracture behavior of micron size A-glass and polyamide (PA6) particle filled epoxy is demonstrated. Filled-epoxy with 3% V_f of PA6 filler is shown to produce the same dynamic fracture toughness enhancement as the one due to 10% V_f glass.

© 2012 Elsevier Ltd. All rights reserved.

1. Introduction

Fracture-resistant, lightweight, toughened materials are desirable in a wide variety of engineering applications. In the past few decades, there has been a great deal of interest in improving fracture toughness of polymers by adding either stiff or compliant filler particles into the matrix. Early works in this regard have been reported by Kinloch et al. (1983a,b, 1994) on deformation and fracture behavior of rubber-toughened epoxies. They performed microstructural and fracture studies on unmodified and CTBN rubber modified epoxies and proposed that localized cavitation at the particle–matrix interface, plastic shear yielding in the matrix and crack-tip blunting are the main sources of energy dissipation and increased toughness in the rubber-modified epoxy. Geisler and Kelley (1994) used rubbery and rigid fillers as well as a combina-

tion of both types to improve fracture toughness of epoxy resins and found that both rubbery and rigid particle-filled epoxies showed higher fracture energies than the neat epoxy. In addition, cured resins prepared with an optimum loading of both rubbery and rigid particles resulted in greater fracture energies than those from rubbery or rigid particles alone. The crack front impedance is said to have toughened the rigid particle composites and localized plastic deformation ahead of the crack front to have contributed in the hybrid composites. Hussain et al. (1996) investigated fracture behavior of particle-filled epoxy composites by varying TiO_2 filler volume fraction and particle size (20 nm and 1 μm) and found that the micron size particles led to higher fracture toughness with increasing volume fraction than the nanoparticles. The work of Tirosh et al. (1995) focused on detailed stress analysis around compliant rubber inclusion particles in a brittle epoxy matrix and a brittle inclusion (styrene–acrylonitrile copolymer, SAN) in a compliant polycarbonate matrix. They found that the tensile strength of a brittle matrix with a soft inclusion continuously degraded as the inclusion size increased whereas the tensile strength of a soft

* Corresponding author. Tel.: +1 334 844 3327; fax: +1 334 844 3307.
   E-mail addresses: jajamkc@auburn.edu (K.C. Jajam), tippuhv@auburn.edu, htippur@eng.auburn.edu (H.V. Tippur).

matrix reinforced with stiff inclusions could be maximized with respect to the matrix properties using optimum particle size. Kitey and Tippur (2005a) examined the role of particle size and filler-matrix adhesion strength on dynamic fracture behavior of glass-filled epoxies. Their work showed that both weakly and strongly bonded filler particles enhanced the steady-state fracture toughness of the composite during crack growth compared to the unfilled epoxy. More interestingly, they observed an optimum particle size for fracture toughness enhancement and noted that weakly bonded filler improved fracture toughness more than the strongly bonded filler during dynamic fracture. The crack front blunting as well as crack front twisting were said to be the dominant toughening mechanisms.

The aforementioned works mainly address the effect of micron size particles (rigid and/or rubbery) on fracture behavior of particulate composites. A few investigations also report fracture studies with macro size fillers of spherical and cylindrical shapes and mostly have been performed under quasi-static loading conditions. Further, most reported studies are analytical (Atkinson, 1972; Cheeseman and Santare, 2000; Erdogan et al., 1974; Kushch et al., 2010; Mantic, 2009; Tamate, 1968) or numerical (Bush, 1998; Eroshkin and Tsukrov, 2005; Kitey et al., 2006; Mogilevskaya and Crouch, 2002, 2004; Savalia et al., 2008) in nature and a rather limited number of experimental works exist. The current work aims to gain a basic understanding on the fracture behavior of particle filler polymers by experimentally investigating interactions between a dynamically growing matrix crack and a stationary stiff or compliant inclusion. One of the very early experimental efforts in this regard dates back to the photoelastic investigation of crack–inclusions under quasi-static loading conditions by O'Toole and Santare (1990). In another quasi-static investigation, Savalia and Tippur (2007) performed an experimental–numerical analysis of crack–inclusion interactions using moiré interferometry and finite element modeling. Among the very few dynamic experimental works in this area, Kitey and Tippur (2008) investigated the dynamic crack growth behavior in the vicinity of an isolated stiff inclusion using coherent gradient sensing (CGS) in conjugation with high-speed photography. CGS being a surface slope detection method, they faced difficulties in analyzing the interferograms satisfactorily when the crack tip was in the vicinity of the inclusion as fringes localized near crack–inclusion interface. In view of this, the authors recently (Jajam and Tippur, 2011) conducted an experimental study of dynamic crack growth past a stiff inclusion by measuring more readily interpretable full-field surface displacements before and after crack–inclusion interaction using a 2D digital image correlation (DIC) technique coupled with high-speed imaging. They also interpreted their measurements using interfacial crack-tip fields when the crack was situated at the crack–inclusion interface. Their work revealed a spike in effective stress intensity factor values and mode-mixity behaviors were consistent with crack attraction and deflection mechanisms. Additionally, the weakly bonded inclusion specimens showed higher fracture surface roughness compared to the strongly bonded ones. This work builds on the previous investigation by the authors and examines the role of elastic mismatch between the matrix and inclusion as well as the interfacial strength between the two during dynamic fracture. The objective of the present work is to perform an optical investigation of dynamic crack growth past stiff and compliant inclusions as a function of inclusion–matrix interfacial strength and the inclusion location relative to the crack under stress wave loading conditions using full-field optical metrology and high-speed photography.

Following this introduction, the basic concept and the approach of the optical methodology used in this work are briefly described. Next, the details of specimen preparation and geometry followed by experimental setup and testing procedure are provided.

Subsequently a description of experimental observations and results in terms of contours of displacements and various fracture parameters such as crack velocity histories, effective stress intensity factor histories, mode-mixity behaviors are presented. The differences in fracture surface morphologies are discussed next. The implications of the current study are then demonstrated by studying the dynamic fracture toughness of particulate composites with stiff (glass) and ductile (PA6) fillers. Finally, the major conclusions of this work are reported.

2. Experimental approach

The 2D DIC method was used to monitor decorated random speckle patterns on a specimen surface during crack growth near embedded inclusions. The gray scale of these image patterns was recorded before and after deformation. The images from the deformed and undeformed sets were paired and analyzed using speckle/image correlation approach. Conceptually, a sub-image in an undeformed image was chosen and its location in the corresponding deformed image was identified and the local displacements of this sub-image were quantified. In this study, an approach developed at Auburn (Kirugulige et al., 2007; Kirugulige and Tippur, 2009; Lee et al., 2009) on a MATLAB™ platform, was used to estimate in-plane surface displacement components. In the first step, displacements were estimated by performing a 2D cross-correlation operation of gray scales in the Fourier domain and the peak of the correlation function detected to a sub-pixel accuracy using bicubic interpolation. This process was repeated for the entire image to obtain full-field in-plane displacements. In the second step, an iterative approach based on nonlinear least-square minimization was used to minimize the 2D cross-correlation function in the spatial domain in order to refine the previously computed displacements. Further details regarding experimental setup and testing procedure are presented in the ensuing sections.

3. Experimental details

3.1. Sample preparation and geometry

A low viscosity epoxy system (Epo-Thin™ from Beuhler, Inc., USA) consisting of Bisphenol-A resin and an amine-based hardener in the ratio of 100:39 was employed as the matrix material. This epoxy system offers low shrinkage and relatively long duration room temperature curing characteristics. Prior to pouring the mixture into the mold, a cylindrical inclusion of diameter, $d = 4$ mm and length equal to the specimen thickness (8.6 mm), was positioned at the center of the mold as shown in Fig. 1a. In this study, inclusions of two different elastic moduli, stiff and compliant relative to the matrix, were used. The former was a borosilicate glass inclusion whereas the latter was a polyurethane inclusion. The physical and measured elastic properties of the matrix and inclusion materials are listed in Table 1. A weak inclusion–matrix interface was created by wiping a thin layer of lubricant on both stiff and compliant inclusion cases. In order to achieve a strong inclusion–matrix adhesion, the glass inclusion was treated with amine-based silane (γ-aminopropyltrimethoxysilane) whereas the polyurethane inclusion surface was roughened using a #1000 grit abrasive paper. It should be noted here that the silane is suitable for enhancing organic to inorganic material interface strength and not suitable for organic to organic material interfaces. Hence, the polyurethane inclusion was not silane treated but roughening of the inclusion surface was found to create a strong interface between polyurethane and epoxy (as demonstrated in later sections). To avoid residual stresses, the material was cured slowly at room
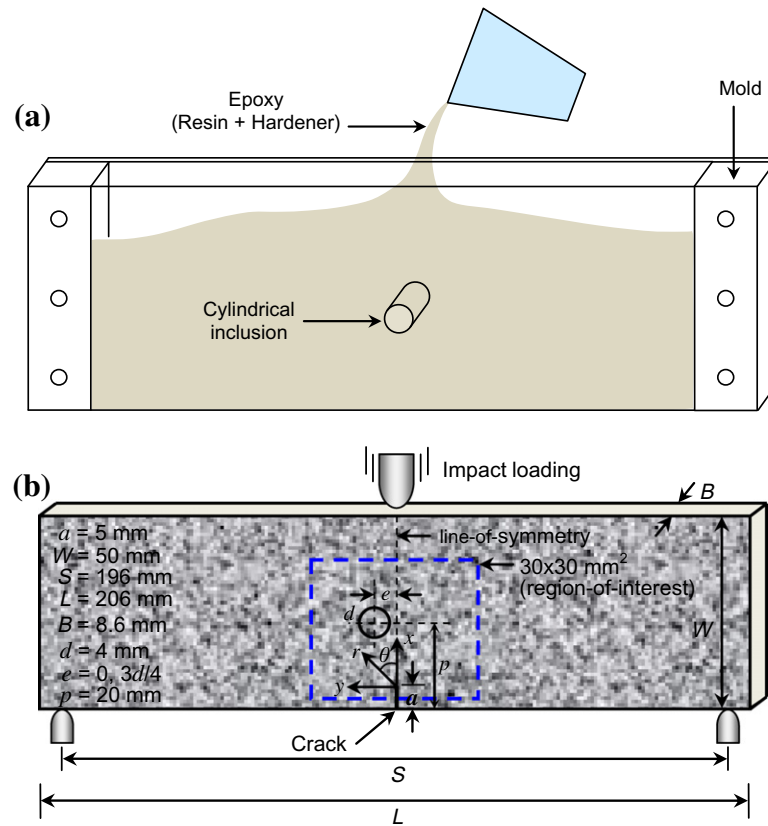
Fig. 1. Specimen details: (a) sample preparation. (b) Specimen geometry and loading configuration with crack-tip coordinate system and inclusion location, with an illustration of random speckle pattern.

Table 1
Material properties of matrix and inclusion.

Material	Density, ρ (kg/m^3)	Elastic modulus, E (GPa)	Longitudinal wave speed, C_L (m/s)	Impedance, (ρC_L) (MPa s/m)	Poisson's ratio, υ
Epoxy[a] (matrix)	1124	3.97	2487	2.79	0.368
Glass[b] (stiff inclusion)	2500	69	5800	14.50	0.190
Polyurethane[a] (compliant inclusion)	1030	0.07	1150	1.18	0.384

[a] In-house measurement (ultrasonic pulse-echo method).
[b] Bourne et al. (1999).

temperature for over 18 h and post-cured at room temperature for 7 days. The cured material was then machined into rectangular coupons of dimensions 206 mm × 50 mm × 8.6 mm. An edge notch of 5 mm in length was cut into the sample using a circular saw of thickness ~300 μm and then the notch tip was sharpened carefully by pressing a sharp razor blade to achieve a relatively quiescent crack initiation and a steady growth before crack–inclusion interaction occurs (Jajam and Tippur, 2011).

The edge cracked fracture specimens were then sprayed with a fine mist of black and white paints alternatively to create a random speckle pattern. Fig. 1b shows the specimen geometry, dimensions and loading configurations with crack-tip coordinate system and inclusion location with an illustration of random speckle pattern on it. The dotted box represents 30 × 30 mm^2 region-of-interest containing the embedded cylindrical inclusion. The line joining the impact point to the crack-tip represents the line-of-symmetry. The location of the inclusion with respect to the initial crack-tip is defined as eccentricity, e, the distance between the inclusion center and the line-of-symmetry. In this work, the inclusion was located at two different eccentricities, $e = 0$ and $3d/4$, being referred to as the symmetric and eccentric (or asymmetric) cases,

respectively. In both cases, the inclusion was positioned at a constant distance of 20 mm from the lower edge of the specimen containing the initial crack.

3.2. Experimental setup

The dynamic experimental setup, shown schematically in Fig. 2, consisted of a drop-tower (Instron-Dynatup 9250HV, USA) for impacting the specimens and a Cordin-550 ultra high-speed digital framing camera (Cordin Scientific Imaging, USA) for recording speckle images in real-time during a fracture event. The drop-tower had an instrumented tup (hemispherical profile) and a pair of anvils for recording force and support reaction histories, respectively. The setup also included instrumentation to produce a delayed trigger pulse when the impactor contacted the specimen ($t = 0$). Two high-energy flash lamps, triggered by the camera and a pulse generator, were employed to illuminate the sample surface. Also, two separate computers were employed, one to record the impact force and anvil reaction histories, and the other to control the high-speed camera and to store the images. The Cordin-550 ultra high-speed digital framing camera is capable of recording
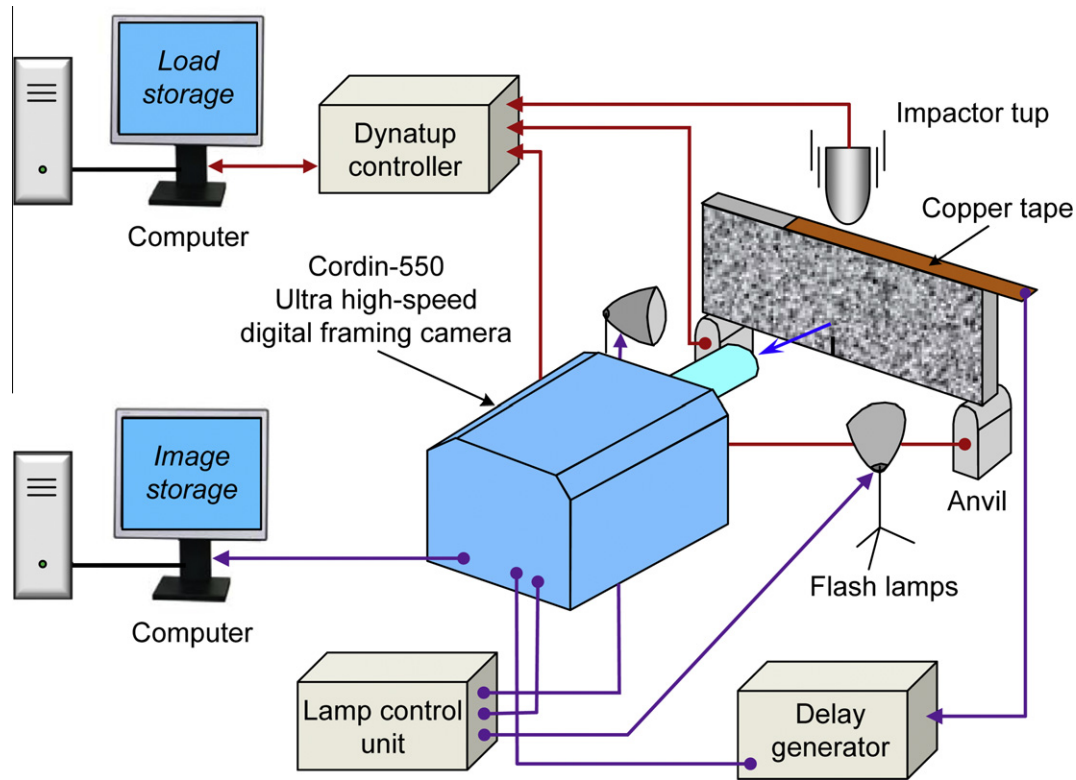
Fig. 2. Schematic of the experimental setup for dynamic fracture study.

images on 32 individual 1000×1000 pixel (pixel size: 7.4 µm square) CCD sensors positioned circumferentially around a five-facet rotating mirror which reflects and sweeps light over these sensors. Additional details about camera performance evaluation and optical calibration can be found in Kirugulige et al. (2007), Kirugulige and Tippur (2009) and Lee et al. (2009).

3.3. Testing procedure

As shown in Fig. 2, the specimen decorated with random speckles was initially rested on two instrumented anvils and the camera was focused on a 30×30 mm² region-of-interest on the specimen in the vicinity of crack-tip and inclusion. Prior to impacting the specimen, a set of 32 images were recorded at a chosen framing rate and stored. While maintaining all camera settings same, another set of 32 images was captured when the specimen was impacted at a velocity of 4.5 m/s. In order to capture the entire fracture event, the images in the case of stiff inclusion specimens were recorded at a framing rate of 300,000 frames per second whereas framing rates ranging from 150,000 to 250,000 frames per second were used for compliant inclusion cases. A total of 32 images were recorded for each undeformed and deformed sets. The corresponding two images of each sensor were paired from undeformed and deformed sets and analyzed. Each resulting image was segmented into sub-images consisting of 24×24 pixels for correlation. While analyzing images, no overlapping of sub-images was used, this resulted in array size of 40×40 data points. Further details regarding image analysis can be found in Jajam and Tippur (2011).

3.4. Evaluation of crack velocity and stress intensity factors (SIFs)

The position of current crack-tip from each digitized image was used to measure the instantaneous values of crack length. The crack velocity (c) was then evaluated from crack length histories using the central difference method by knowing crack growth history from the images,

$$c_i = \left(\frac{da}{dt}\right)_i = \frac{a_{i+1} - a_{i-1}}{t_{i+1} - t_{i-1}} \tag{1}$$

where a and t are crack length and time respectively at a given instant i.

The mode-I and mode-II stress intensity factors (SIFs) were evaluated by an over-deterministic least-squares analysis of crack-opening and crack-sliding displacements, respectively. The governing asymptotic expressions for crack-opening (v) and crack-sliding (u) displacement fields near the tip of a dynamically loaded stationary or steadily growing bimaterial interface crack are given by Deng (1993),

$$\begin{Bmatrix} u(r,\theta) \\ v(r,\theta) \end{Bmatrix} = \sum_{n=0}^{\infty} r^{\frac{n+1}{2}} \frac{\mathrm{Re}[\eta_n^I (K_I)_n r^{i\varepsilon_n}]}{\sqrt{2\pi}} \begin{Bmatrix} u_n^I(\theta) \\ v_n^I(\theta) \end{Bmatrix} + \sum_{n=0}^{\infty} r^{\frac{n+1}{2}} \frac{\mathrm{Im}[\eta_n^{II} (K_{II})_n r^{i\varepsilon_n}]}{\sqrt{2\pi}} \begin{Bmatrix} u_n^{II}(\theta) \\ v_n^{II}(\theta) \end{Bmatrix} \tag{2}$$

where r and θ are the polar coordinates defined at the current crack-tip, $\varepsilon_n = \varepsilon$, $\eta_n^I = 1$, and $\eta_n^{II} = \eta$ when $n = 0, 2, 4, \ldots$, and $\varepsilon_n = 0$, $\eta_n^I = \eta$, and $\eta_n^{II} = 1$ when $n = 1, 3, 5, \ldots$, ε is the oscillation index, η is the mismatch parameter. In Eq. (2), terms corresponding to $n = 0$ provide the oscillatory singular crack-tip fields and the coefficients[1] of $(K_I)_n$ and $(K_{II})_n$ of the dominant terms ($n = 0$) are the dynamic SIFs, respectively. In this work, SIF values were extracted using dominant terms ($n = 0$) at crack initiation and in the post-initiation regime, therefore, explicit expressions for displacement fields for steadily

---

[1] Subscripts and superscripts *I* and *II* are used instead of traditional 1 and 2 notation for ease of transitioning from bimaterial fracture mechanics equations to the homogeneous ones.

growing interface cracks in dissimilar isotropic materials were employed (Deng, 1993):

$$u_n^I(\theta) = \frac{1}{\mu D[(n+1)^2 + 4\varepsilon^2]\cosh\pi\varepsilon} \left\{ \begin{array}{l} (n+1)[C_1(n+2,\varepsilon,\eta) + C_1(n+2,-\varepsilon,-\eta)] \\ -2\varepsilon[S_1(n+2,\varepsilon,\eta) - S_1(n+2,-\varepsilon,-\eta)] \\ +\alpha_2(n+1)[C_2(n+2,\varepsilon,\eta) + C_2(n+2,-\varepsilon,-\eta)] \\ -2\alpha_2\varepsilon[S_2(n+2,\varepsilon,\eta) - S_2(n+2,-\varepsilon,-\eta)] \end{array} \right\}$$
(3)

$$u_n^{II}(\theta) = \frac{1}{\eta\mu D[(n+1)^2 + 4\varepsilon^2]\cosh\pi\varepsilon} \left\{ \begin{array}{l} (n+1)[S_1(n+2,\varepsilon,\eta) - S_1(n+2,-\varepsilon,-\eta)] \\ +2\varepsilon[C_1(n+2,\varepsilon,\eta) + C_1(n+2,-\varepsilon,-\eta)] \\ +\alpha_2(n+1)[S_2(n+2,\varepsilon,\eta) - S_2(n+2,-\varepsilon,-\eta)] \\ +2\alpha_2\varepsilon[C_2(n+2,\varepsilon,\eta) + C_2(n+2,-\varepsilon,-\eta)] \end{array} \right\}$$
(4)

$$v_n^I(\theta) = \frac{1}{\mu D[(n+1)^2 + 4\varepsilon^2]\cosh\pi\varepsilon} \left\{ \begin{array}{l} \alpha_1(n+1)[S_1(n+2,\varepsilon,\eta) + S_1(n+2,-\varepsilon,-\eta)] \\ -2\alpha_1\varepsilon[-C_1(n+2,\varepsilon,\eta) + C_1(n+2,-\varepsilon,-\eta)] \\ +(n+1)[S_2(n+2,\varepsilon,\eta) + S_2(n+2,-\varepsilon,-\eta)] \\ -2\varepsilon[-C_2(n+2,\varepsilon,\eta) + C_2(n+2,-\varepsilon,-\eta)] \end{array} \right\}$$
(5)

$$v_n^{II}(\theta) = \frac{1}{\eta\mu D[(n+1)^2 + 4\varepsilon^2]\cosh\pi\varepsilon} \left\{ \begin{array}{l} \alpha_1(n+1)[-C_1(n+2,\varepsilon,\eta) + C_1(n+2,-\varepsilon,-\eta)] \\ +2\alpha_1\varepsilon[S_1(n+2,\varepsilon,\eta) + S_1(n+2,-\varepsilon,-\eta)] \\ +(n+1)[-C_2(n+2,\varepsilon,\eta) + C_2(n+2,-\varepsilon,-\eta)] \\ +2\varepsilon[S_2(n+2,\varepsilon,\eta) + S_2(n+2,-\varepsilon,-\eta)] \end{array} \right\}$$
(6)

where

$$C_1(n,\varepsilon,\eta) = -r_1^{(n-1)/2} e^{\varepsilon(\pi-\theta_1)}[2\alpha_2\eta - (1+\alpha_2^2)]\cos\left(\frac{n-1}{2}\theta_1 + \varepsilon\ln r_1\right)$$

$$S_1(n,\varepsilon,\eta) = r_1^{(n-1)/2} e^{\varepsilon(\pi-\theta_1)}[2\alpha_2\eta - (1+\alpha_2^2)]\sin\left(\frac{n-1}{2}\theta_1 + \varepsilon\ln r_1\right)$$

$$C_2(n,\varepsilon,\eta) = -r_2^{(n-1)/2} e^{\varepsilon(\pi-\theta_2)}[2\alpha_1 - \eta(1+\alpha_2^2)]\cos\left(\frac{n-1}{2}\theta_2 + \varepsilon\ln r_2\right)$$

$$S_2(n,\varepsilon,\eta) = r_2^{(n-1)/2} e^{\varepsilon(\pi-\theta_2)}[2\alpha_1 - \eta(1+\alpha_2^2)]\sin\left(\frac{n-1}{2}\theta_2 + \varepsilon\ln r_2\right)$$

$$r_m = \sqrt{x^2 + \alpha_m^2 y^2}, \quad \theta_m = \tan^{-1}\left(\frac{\alpha_m y}{x}\right), \quad m = 1, 2,$$

$$\alpha_1 = \sqrt{1 - \left(\frac{c}{C_L}\right)^2}, \quad \alpha_2 = \sqrt{1 - \left(\frac{c}{C_S}\right)^2}$$

$$C_L = \sqrt{\frac{(\kappa+1)\mu}{(\kappa-1)\rho}}, \quad C_S = \sqrt{\frac{\mu}{\rho}}, \quad \kappa = \frac{3-\upsilon}{1+\upsilon} \quad \text{for plane stress}$$

$$D = 4\alpha_1\alpha_2 - (1+\alpha_2^2)^2, \quad \varepsilon = \frac{1}{2\pi}\ln\frac{1-\beta}{1+\beta}$$
(7)

In the above equations, (x,y) are the instantaneous Cartesian coordinates situated at the current crack-tip, c is the crack-tip velocity, C_L and C_S are longitudinal and shear wave speeds, ρ is the mass density, β is one of the two Dundurs' elastic mismatch parameters, μ and υ are shear modulus and Poisson's ratio, respectively. Further, Eqs. (3)–(7) can be reduced to the form of a dynamically loaded stationary crack in the limit the crack velocity $c \to 0$. Moreover, when the oscillation index ε becomes zero, the bimaterial equations reduce to the ones for the homogeneous case. Thus, these equations can be used to extract crack-tip parameters over the entire history of crack growth during fracture event.

In order to extract SIF history, the crack-opening and crack-sliding displacement fields were digitized by identifying the current crack-tip location. The displacement data used in the analysis was collected in the vicinity of the crack-tip and limited to the region $0.3 < r/B < 1.5$ and ($-150° \leqslant \theta \leqslant -90°$ and $90° \leqslant \theta \leqslant 150°$) as it has been shown that 3D deformations are minimum in this region (Tippur et al., 1991). At each data point, v and u displacement

values as well as the location of these points were stored. The digitized data were used in Eq. (2) along with an over-deterministic least-squares analysis scheme in order to estimate the two SIFs. This process was carried out for all 32 image pairs and the SIF histories were generated. Due to mixed-mode crack growth in the inclusion vicinity, the SIFs were used to evaluate an effective SIF, K_e, and mode-mixity, ψ, as,

$$K_e = \sqrt{K_I^2 + K_{II}^2} = \sqrt{K_1^2 + K_2^2}$$
(8)

$$\psi = \tan^{-1}\left(\frac{K_{II}}{K_I}\right) \quad \text{or} \quad \tan^{-1}\left(\frac{K_2}{K_1}\right) \quad \text{or} \quad \tan^{-1}\left(\frac{\text{Im}(Ka^{i\varepsilon})}{\text{Re}(Ka^{i\varepsilon})}\right)$$
(9)

where a is a length parameter, chosen to be unity in this study, and ε is the oscillation index as defined previously. In this work, the value of ε ranges from 0.096 to 0.156 for the stiff inclusion and -0.0886 for the compliant inclusion for interface crack growth as a function of crack-tip velocity at the inclusion–matrix interface and zero for crack propagation in the matrix.

4. Experimental results

4.1. Crack path and surface deformation histories

The pre-notched fracture specimens embedded with weakly and strongly bonded symmetric ($e = 0$) and eccentric ($e = 3d/4$), stiff and compliant inclusions were subjected to symmetric impact loading. Photographs of eight fractured samples from each configuration representing different crack–inclusion interaction scenarios are shown in Fig. 3. The impact occurs on the top edge of each image and the initial crack-tip is at the bottom edge as indicated. The location of cylindrical inclusion is shown by a dotted circle and the vertical broken arrow indicates the direction of crack propagation (in all the photographs in Fig. 3, it can be seen that just before the upper edge of the specimens, the crack path deviates noticeably due to a combination of free-edge and impact point interactions). In each configuration, the crack propagates self-similarly until it reached the inclusion–matrix interface vicinity and significant differences in crack paths occur subsequently and are discussed in the following sections.

4.1.1. Weakly bonded stiff and compliant inclusions ($e = 0$)
The crack trajectories for the cases of symmetrically located weakly bonded stiff and compliant inclusions ($e = 0$) are shown in Fig. 3a and b. In both cases, it can be seen that once inclusion–matrix interface debonded, the crack was momentarily arrested after it circumscribed the interface covering a distance of approximately half the inclusion circumference. In the case of stiff inclusion, the crack reinitiated in a mode-I fashion with approximately zero offset distance with respect to the initial crack path whereas high frequency irregularity in the crack path can be noticed in the compliant case. These features in the latter indicate greater energy dissipation for compliant inclusion compared to the stiff one.

4.1.2. Strongly bonded stiff and compliant inclusions ($e = 0$)
Figs. 3c and d show crack growth behavior for the cases of symmetrically located and strongly bonded stiff and compliant inclusions ($e = 0$). Initially, the crack was arrested in both stiff and compliant cases as it approached the inclusion vicinity. The crack circumvented the inclusion in both cases but to a lesser extent in the stiff inclusion compared to the compliant one and then deflected away from inclusion–matrix interface, nearly tangentially, before propagating in a nearly mode-I fashion. After crack–inclusion interaction, the crack propagated at an offset of about half the inclusion diameter in the stiff inclusion case compared to the
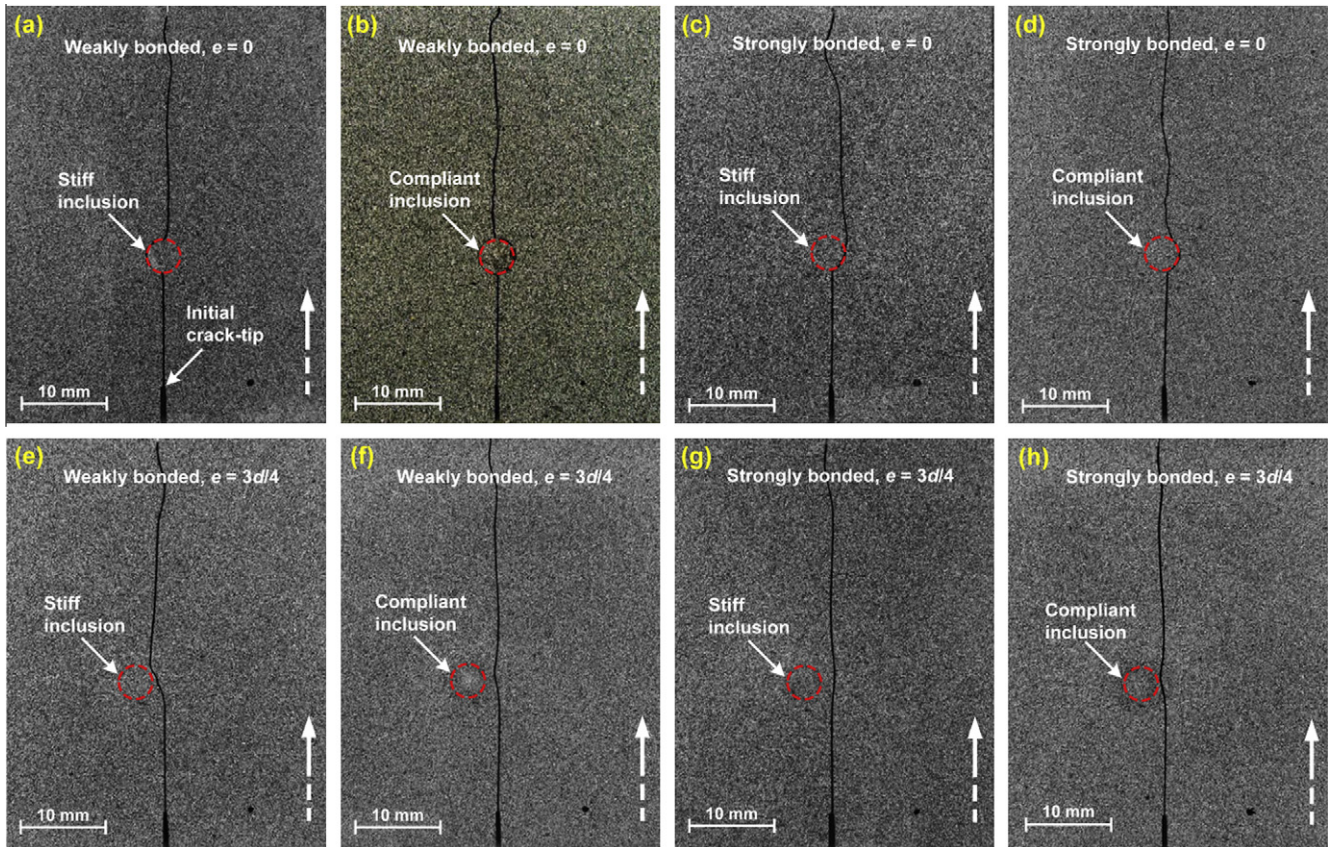
Fig. 3. Photographs of fractured stiff and compliant inclusion specimens showing different crack–inclusion interaction scenarios: (a) Weakly bonded stiff inclusion ($e = 0$). (b) Weakly bonded compliant inclusion ($e = 0$). (c) Strongly bonded stiff inclusion ($e = 0$). (d) Strongly bonded compliant inclusion ($e = 0$). (e) Weakly bonded stiff inclusion ($e = 3d/4$). (f) Weakly bonded compliant inclusion ($e = 3d/4$). (g) Strongly bonded stiff inclusion ($e = 3d/4$). (h) Strongly bonded compliant inclusion ($e = 3d/4$). The black dot adjacent to initial crack-tip denotes the reference mark and the broken arrow indicates crack propagation direction.

compliant one. Similar to the weakly bonded compliant inclusion case, the crack path in the strongly bonded case also shows high frequency irregularity in crack path hinting at a higher energy dissipation (see Fig. 3b and d).

4.1.3. Weakly bonded stiff and compliant inclusions ($e = 3d/4$)

When the inclusion is not in the prospective crack path but positioned eccentrically ($e = 3d/4$), the crack trajectories in the vicinity of the inclusion are different when compared to the symmetrically located inclusion case. Figs. 3e and f show crack paths for weakly bonded stiff and compliant eccentric cases. In case of the stiff inclusion, it is clearly evident that the crack was attracted towards the weak inclusion–matrix interface and left the inclusion vicinity and tended to follow the initial crack path, whereas in the compliant case, as the crack approached the inclusion vicinity, it was attracted by the inclusion and to a lesser extent when compared to the stiff inclusion case. Subsequently the crack propagated along a mode-I path.

4.1.4. Strongly bonded stiff and compliant inclusions ($e = 3d/4$)

The eccentric cases for strongly bonded stiff and compliant inclusions are shown in Fig. 3g and h, respectively. It is interesting to note that eccentric cases show opposite crack trajectories when bonded strongly. From Fig. 3g, it can be seen that as the crack approached the inclusion vicinity, the stronger inclusion–matrix interface in the stiff case forced the crack to deflect away from the inclusion before returning to a nominally mode-I path. On the other hand, as shown in Fig. 3h, the crack was attracted by

the compliant inclusion even for a strong inclusion–matrix bonding.

A selected speckle image of 30×30 mm^2 region-of-interest from each experiment is shown in Fig. 4. The time instant (t) at which the images were recorded after impact is shown on each image and the arrow indicates the current crack-tip position. Note that in Fig. 4, the speckle images are shown at nearly the same time instant ($t \approx 192$ µs) except in two cases due to slightly different recording rates used. From Figs. 3 and 4, it is worth noting the effects of inclusion stiffness, inclusion eccentricity and inclusion–matrix adhesion strength on crack trajectories. For symmetrically located inclusion ($e = 0$) cases, the crack front was momentarily trapped at the weak interface compared to the stronger one in the stiff inclusion case, whereas in both weakly and strongly bonded compliant inclusion specimens, the crack experienced a substantial crack arrest event. In the eccentric inclusion ($e = 3d/4$) cases, the crack was clearly attracted by the weak inclusion–matrix interface whereas the strong inclusion–matrix interface led to crack deflection in the stiff inclusion cases. On the other hand, in the compliant inclusion specimens, the crack was attracted by both weak and strong inclusion–matrix interfaces.

Two representative speckle images (rotated clockwise by 90° relative to Fig. 4) along with the corresponding full-field crack-opening (v-field or displacement along the y-axis) and crack-sliding (u-field or displacement along the x-axis) displacement contours for weakly bonded stiff and strongly bonded compliant inclusion specimens at eccentricity $e = 0$ are shown in Fig. 5. In this work, displacements were obtained as a matrix of 40×40 data points in the inclusion–matrix vicinity for each image pair and
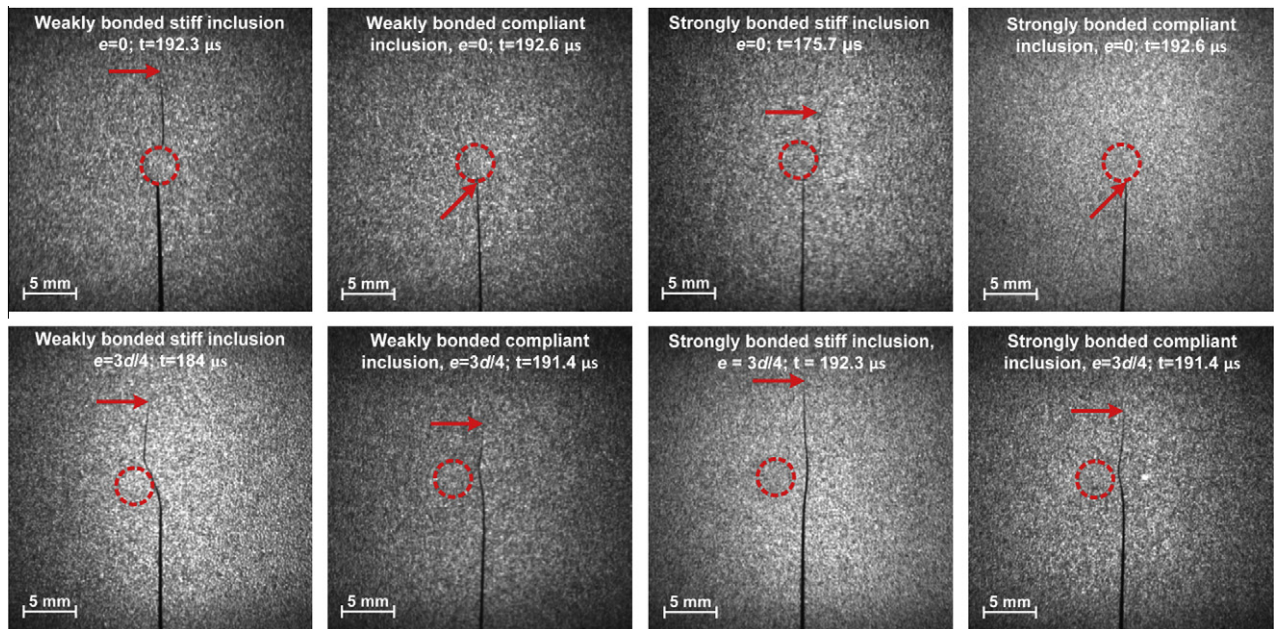
Fig. 4. Selected speckle images of 30×30 mm² region-of-interest at different time instants recorded by Cordin-550 ultra high-speed digital camera. The dotted circle represents inclusion location and arrow indicates current crack-tip position.
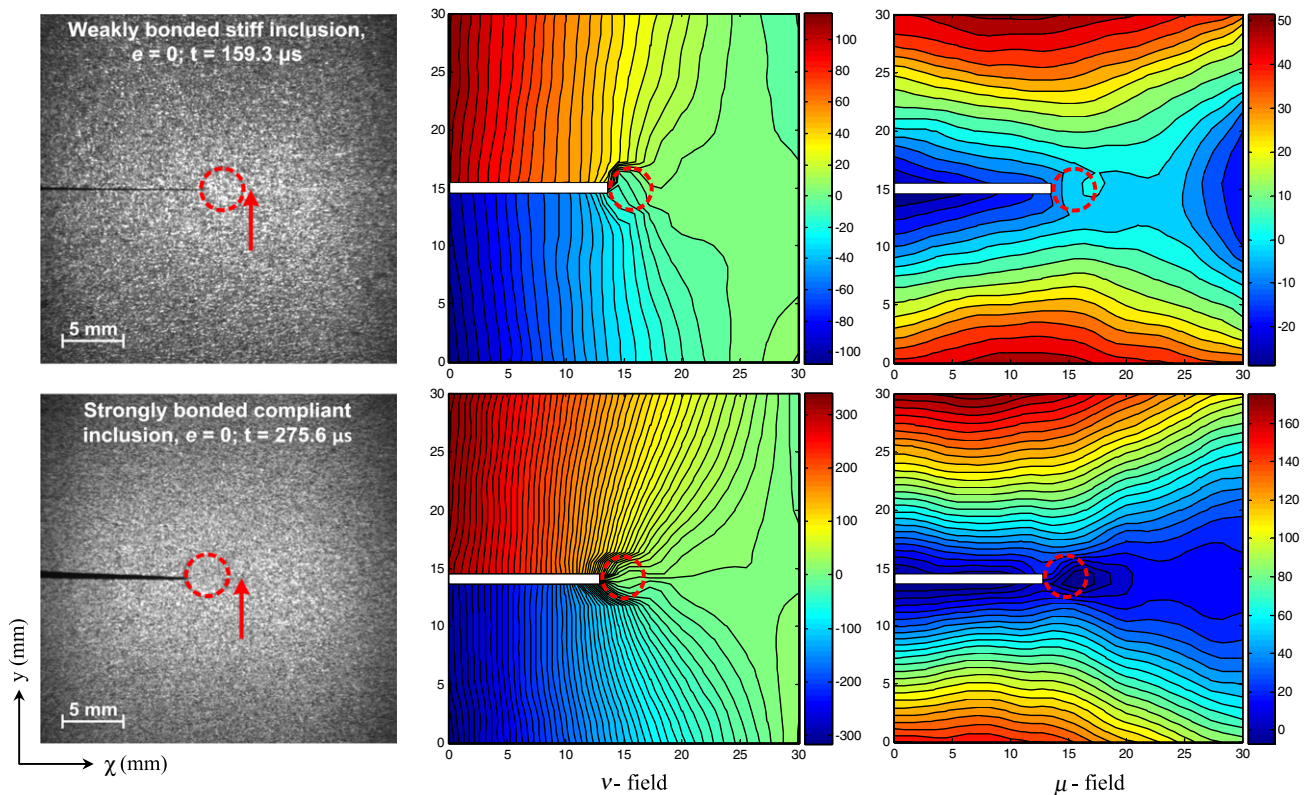
Fig. 5. Representative speckle images of 30×30 mm² region-of-interest for weakly bonded stiff inclusion and strongly bonded compliant inclusion specimens at eccentricity, $e = 0$ with full-field crack-opening (v-field) and crack-sliding (u-field) displacement contours (contour interval: 5 μm for stiff and 7 μm for compliant inclusion specimens). Color-bars indicate displacements in μm. The location of cylindrical inclusion is represented by dotted circle and arrow indicates the current crack-tip position in the speckle images. (For interpretation of the references to color in this legend, the reader is referred to the web version of this article.)

full-field displacement contours with 5 μm (stiff inclusion) and 7 μm (compliant inclusion) intervals are shown. In the v-field, contour lines (magnitude) are symmetric relative to the crack path before the crack interacts with the inclusion suggesting dominant mode-I conditions. The discontinuity in displacements around the inclusion can be seen when the crack reaches the inclusion. Also, perturbations in contour lines in the inclusion vicinity become more prominent as debonding of the inclusion occurs in both
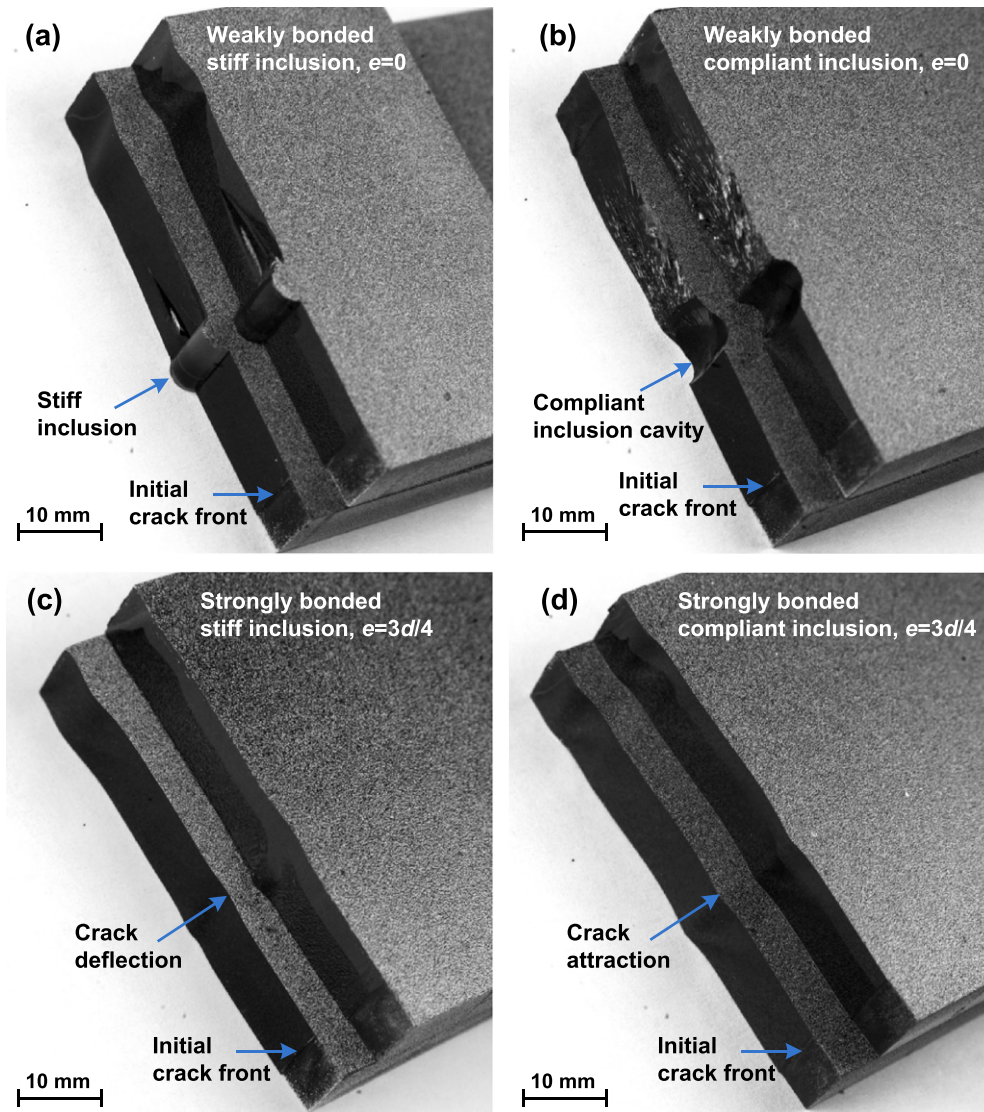
Fig. 6. Right-half ligaments of fractured stiff and compliant inclusion specimens from multiple experiments demonstrating experimental repeatability: (a) weakly bonded stiff inclusion ($e = 0$). (b) Weakly bonded compliant inclusion ($e = 0$). (c) Strongly bonded stiff inclusion ($e = 3d/4$). (d) Strongly bonded compliant inclusion ($e = 3d/4$).

cases. It should be noted that the contours lines within the stiff inclusion are nearly parallel to each other and equally spaced implying rigid rotation of the inclusion after debonding,[2] whereas in the compliant inclusion, the isolines show non-uniformity and hence straining of the inclusion due to compliancy. This difference in the inclusion deformations was confirmed by performing quasi-static experiments carried out on three-point bend specimens with stiff and compliant inclusions near a stationary crack. Some of the experimental details are included in Appendix A for completeness.

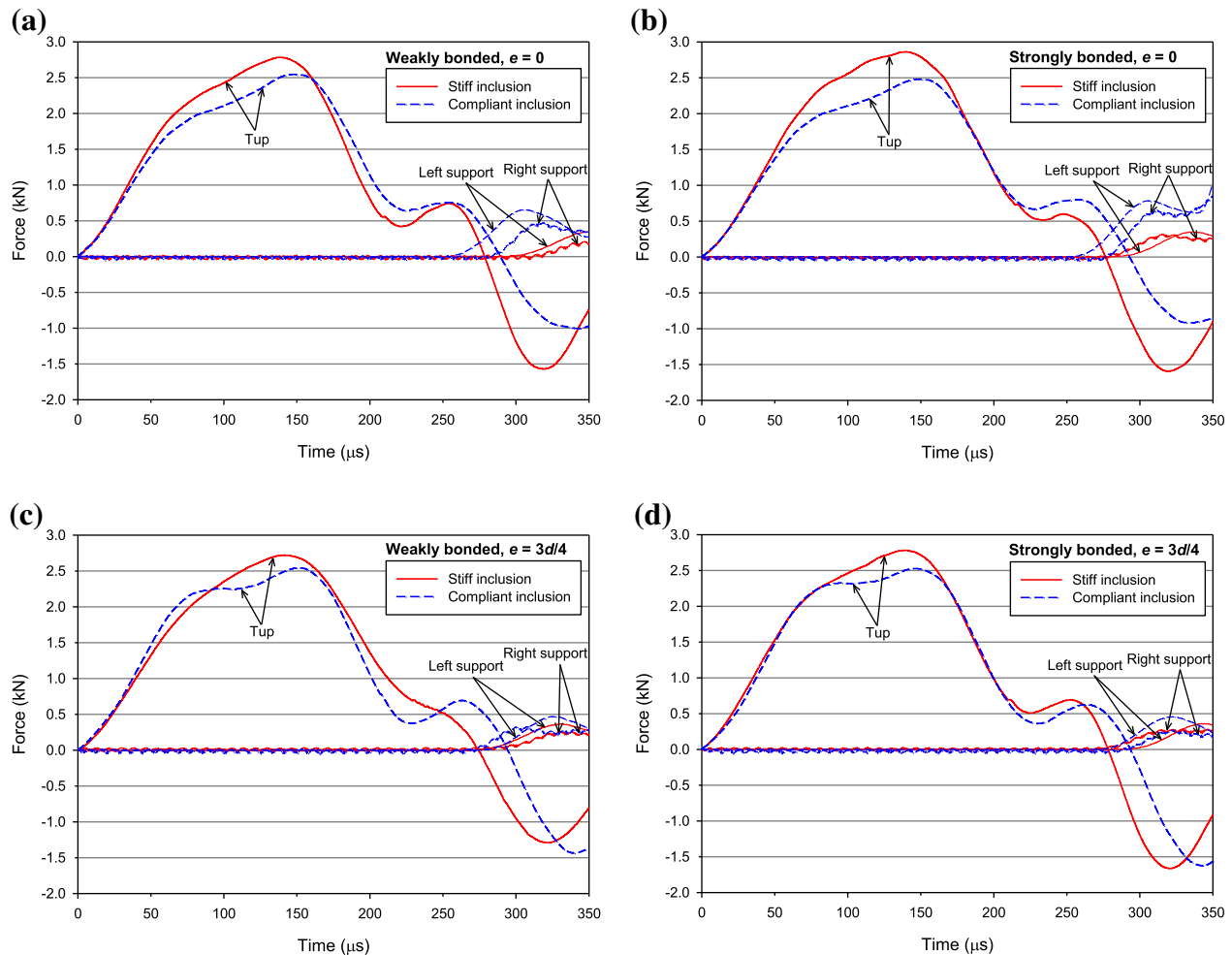### 4.2. Experimental repeatability

To ensure repeatability in the observed fracture behavior multiple experiments (2–3 specimens per configuration) were performed for both stiff and compliant inclusion cases at eccentricities $e = 0$, $3d/4$ as well as the two adhesion strengths. A

few cases are shown in Fig. 6. Figs. 6a–d show right-half ligaments of two fractured stiff and compliant inclusion specimens for each weakly bonded ($e = 0$) and strongly bonded ($e = 3d/4$) configurations. A rather high degree of reproducibility in crack paths including several macroscale surface features is clearly evident. More importantly, distinctly different crack–inclusion interaction scenarios can be seen in these four configurations. The ligaments holding glass inclusions in Fig. 6a show good repeatability in the crack path selection. An excellent repeatability in fractured surface ruggedness is also quite evident in weakly bonded compliant inclusion specimens in Fig. 6b. The crack deflection is clearly visible in each ligament shown in Fig. 6c whereas crack attraction by the compliant inclusion can be seen in Fig. 6d. Also, the photographs in Fig. 6 demonstrate that the crack propagated in a dominant mode-I fashion *before* and *after* the encounter with the inclusion. Thus, similarity of crack growth behavior, surface roughness, and crack attraction and deflection mechanisms in multiple samples indicates the robustness and repeatability of experiments reported in this study.

The tup and anvil load histories were recorded for each experiment and are shown in Fig. 7 for weakly and strongly bonded stiff and compliant inclusion specimens. The crack initiated at about

---

[2] Note that despite the camera being a state-of-the-art instrument, the spatial resolution is still far from being optimum for this study. This limits the ability to capture deformation details accurately near the interface without magnifying the image. If magnified, however, the information regarding global deformations will be greatly compromised and hence not used in this work.

(a)

(b)

(c)

(d)

Fig. 7. Impactor force and support reaction histories recorded by Instron Dynatup 9250HV drop tower for stiff and compliant inclusion specimens: (a) Weakly bonded ($e = 0$). (b) Strongly bonded ($e = 0$). (c) Weakly bonded ($e = 3d/4$). (d) Strongly bonded ($e = 3d/4$). (Note that the tup forces are shown as positive instead of negative.)

120 and 135 μs and complete fracture of the specimen occurred in about 220 and 300 μs after impact in stiff and compliant inclusion specimens, respectively. Thus, only the dominant peak of the tup load history is significant. From Fig. 7a–d, note that the peak impact force (compressive) recorded by the tup in the stiff inclusion specimens is higher than the compliant ones. The reaction histories were captured by the two instrumented anvils and it can be seen that supports feel the reaction force only after 300 μs by which time the crack had already traversed the entire specimen width. This shows that reaction forces from support anvils do not contribute to the crack initiation and growth in the specimens, suggesting that a free–free cracked beam should suffice analytical or computational modeling of these experiments in the future.

4.3. Crack growth histories

The crack length histories for each specimen configuration are plotted[3] in Fig. 8. In this plot, the crack-initiation is denoted by $t - t_i = 0$ so that the positive and negative values correspond to the post-initiation and pre-initiation periods, respectively. Here t_i

indicates the time at crack-initiation after impact. The region between the two vertical broken lines *qualitatively* suggests the duration of crack–inclusion interaction.

Figs. 8a and b show crack length histories for weakly and strongly bonded, symmetrically located ($e = 0$), stiff and compliant inclusion specimens, respectively. In the stiff inclusion case (see Fig. 8a), following initiation, a monotonic crack growth is evident and as the crack approached the inclusion, the rate of crack extension drops modestly before increasing at a much faster rate in the crack–inclusion vicinity as it gets attracted by the interface. Unlike the weakly bonded inclusion case, the crack growth is slower in the region *before* the crack interacts with the strongly bonded inclusion and in the inclusion vicinity an abrupt jump in crack length can be noticed but this jump is lower than the one for the weakly bonded case. The crack is momentarily arrested at the inclusion–matrix interface before it continues to grow again. As it leaves the inclusion vicinity, the crack grows at the same rate in both weakly and strongly bonded inclusion cases. On the other hand, in Fig. 8b it is interesting to note that after initiation the crack propagates steadily before it interacts with the compliant inclusion and then the crack growth ceases at inclusion–matrix interface for about 60 and 100 μs in the case of weakly and strongly bonded compliant inclusion, respectively. Note that, this is about a third to a half of the total observation window. Subsequently, the crack reinitiates much earlier and

---

[3] In this work, the inter frame time varies due to different framing rates employed for stiff (300,000 fps) and compliant (150,000–250,000 fps) inclusion experiments. Hence, for clarity, the fracture parameters for stiff and compliant inclusion specimens are plotted separately instead of plotting on the same graph.
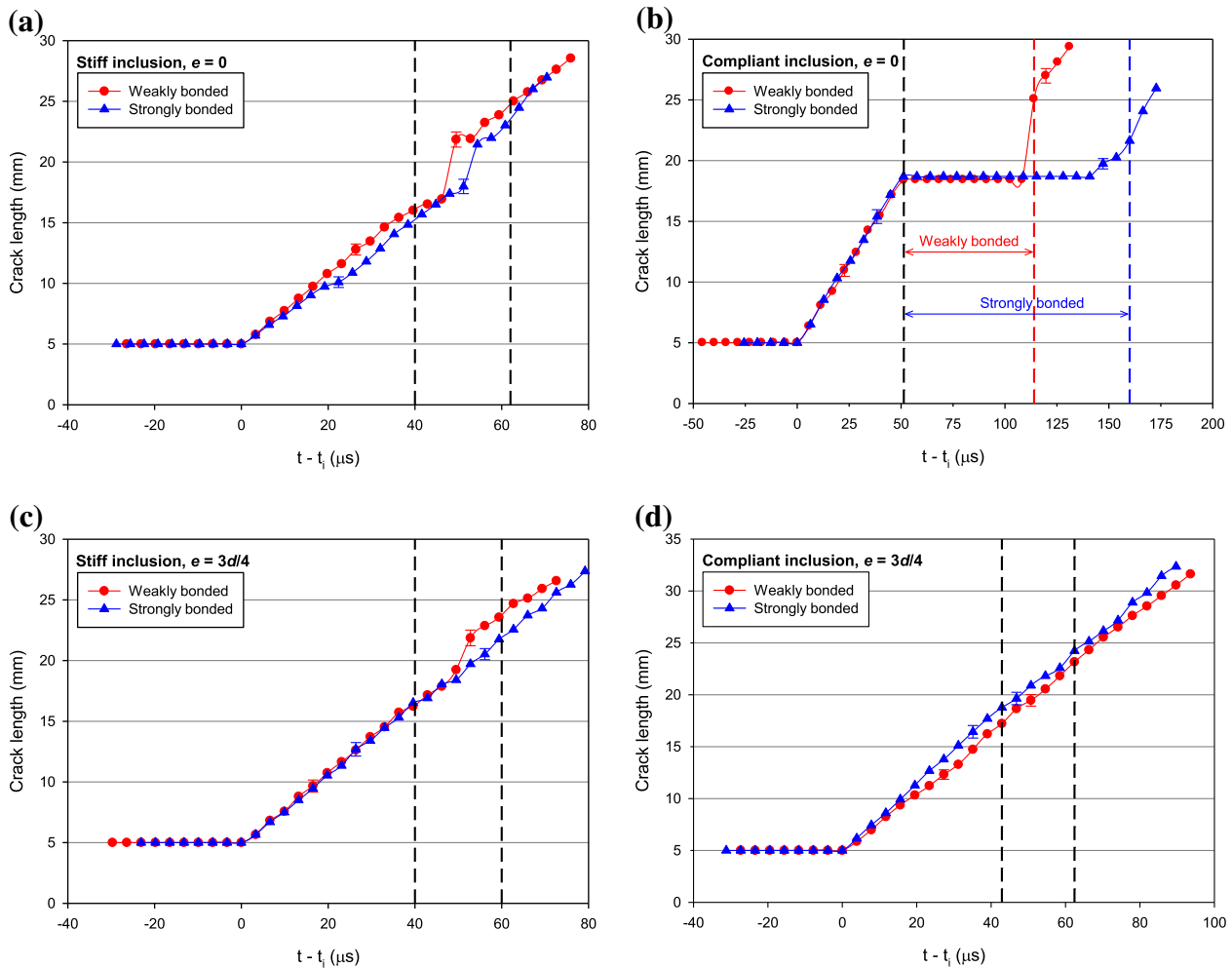
Fig. 8. Crack length histories for weakly and strongly bonded inclusion specimens: (a) Stiff inclusion ($e = 0$). (b) Compliant inclusion ($e = 0$). (c) Stiff inclusion ($e = 3d/4$). (d) Compliant inclusion ($e = 3d/4$). The region between vertical broken lines represents crack–inclusion vicinity.

faster in the weakly bonded case when compared to the strongly bonded one followed by a monotonic propagation until complete fracture.

The crack length histories when the stiff and compliant inclusions are located eccentrically ($e = 3d/4$) are shown in Fig. 8c and d, respectively. In Fig. 8c it can be seen that, in stiff inclusions specimens, before the crack reaches the inclusion vicinity it grows at a constant rate and the crack extension histories for both weakly and strongly bonded inclusion cases coincide. In the crack–inclusion vicinity and beyond, the weakly bonded inclusion shows a faster crack growth compared to the strongly bonded counterpart in which crack growth remains nominally undisturbed. On the contrary, in case of the compliant inclusion specimens as depicted in Fig. 8d, crack growth is slow in the weakly bonded case compared to the strongly bonded one and crack extension histories do not coincide throughout the fracture event.

The instantaneous values of crack lengths were subsequently used to estimate crack velocity histories and are plotted in Fig. 9. The effect of the type of inclusion and adhesion strength on crack velocity can be seen in these plots for both inclusion eccentricities. In Fig. 9a, the symmetrically located ($e = 0$) stiff inclusion cases show nearly similar velocity profiles (300 m/s) until the crack encounters the inclusion. A drop in velocity can be seen in both weakly and strongly bonded inclusions as the crack slows near inclusion–matrix interface just before re-initiation. The crack velocity drops to ∼100 m/s and 210 m/s for weakly and strongly

bonded inclusions, respectively. Subsequently, velocities in weakly and strongly bonded inclusions reach ∼800 m/s and ∼600 m/s, respectively, before the crack attains a steady velocity of ∼300 m/s in both cases. Fig. 9b shows crack growth histories of weakly and strongly bonded compliant inclusion specimens. Upon initiation, crack accelerates and reaches a relatively steady velocity of ∼300 m/s for about 50 μs and then decelerates when it encounters the compliant inclusion and gets completely stalled at the inclusion–matrix interface for about 60 and 100 μs for weakly and strongly bonded inclusions, respectively. Following this, the crack reinitiates with a velocity of ∼600 m/s and accelerates to a velocity of ∼780 m/s before slowing to ∼300 m/s in the weakly bonded case. On the other hand, for strongly bonded inclusion, the crack reinitiated more slowly to reach ∼300 m/s in the observation window.

Figs. 9c and d show velocity data for weakly and strongly bonded stiff and compliant inclusion specimens, respectively, when the inclusion is placed eccentrically ($e = 3d/4$). Again, the velocity profiles are nearly similar until the crack reaches in the inclusion vicinity. In Fig. 9c it can been seen that for the weakly bonded case the maximum velocity reaches ∼600 m/s as the crack is initially attracted and trapped at the inclusion by the weak interface, whereas a constant decrease in velocity can be seen for the strongly bonded case as the crack circumvents the inclusion. On the other hand, in the case of compliant inclusion specimens (Fig. 9d), the crack propagates relatively slowly in the weakly
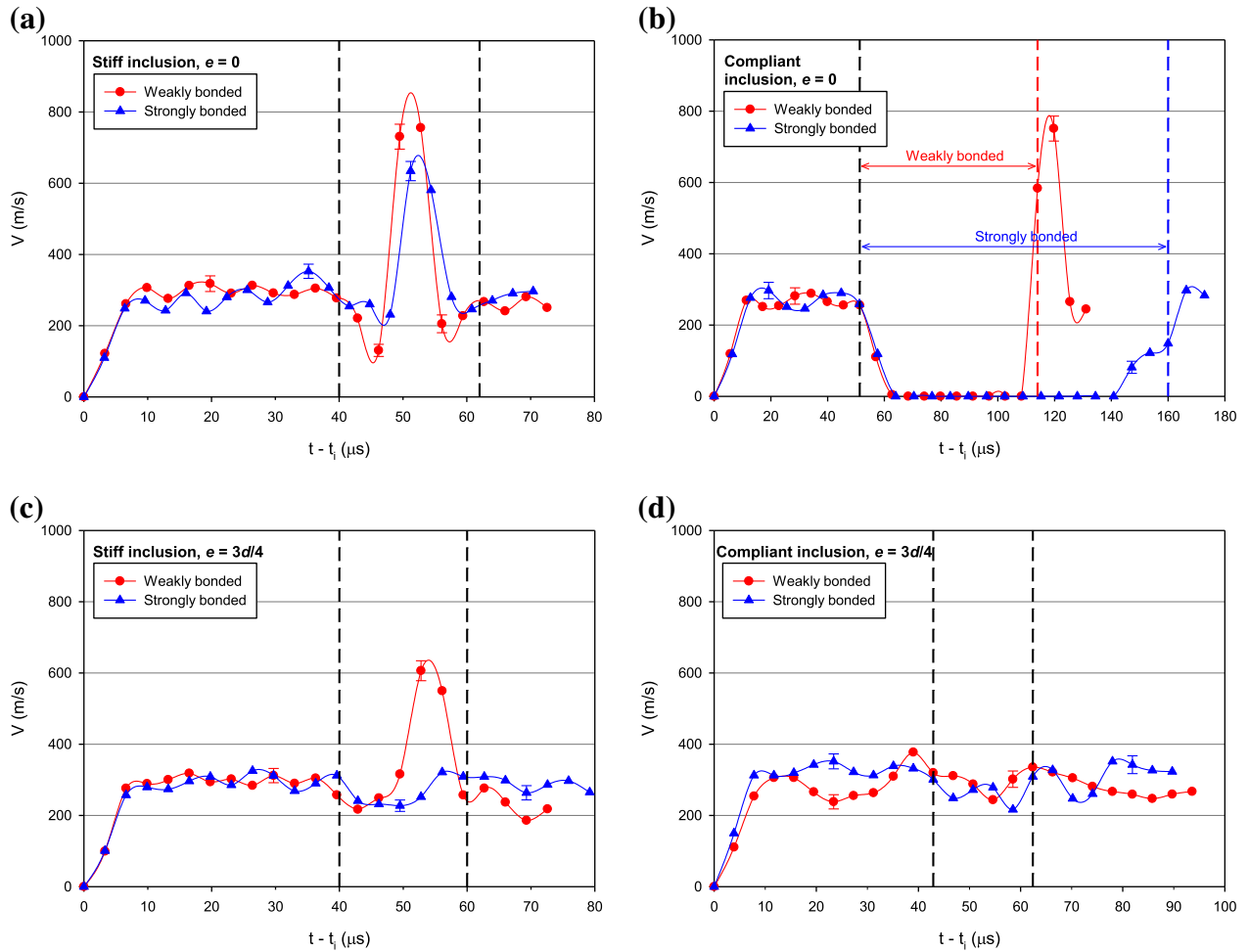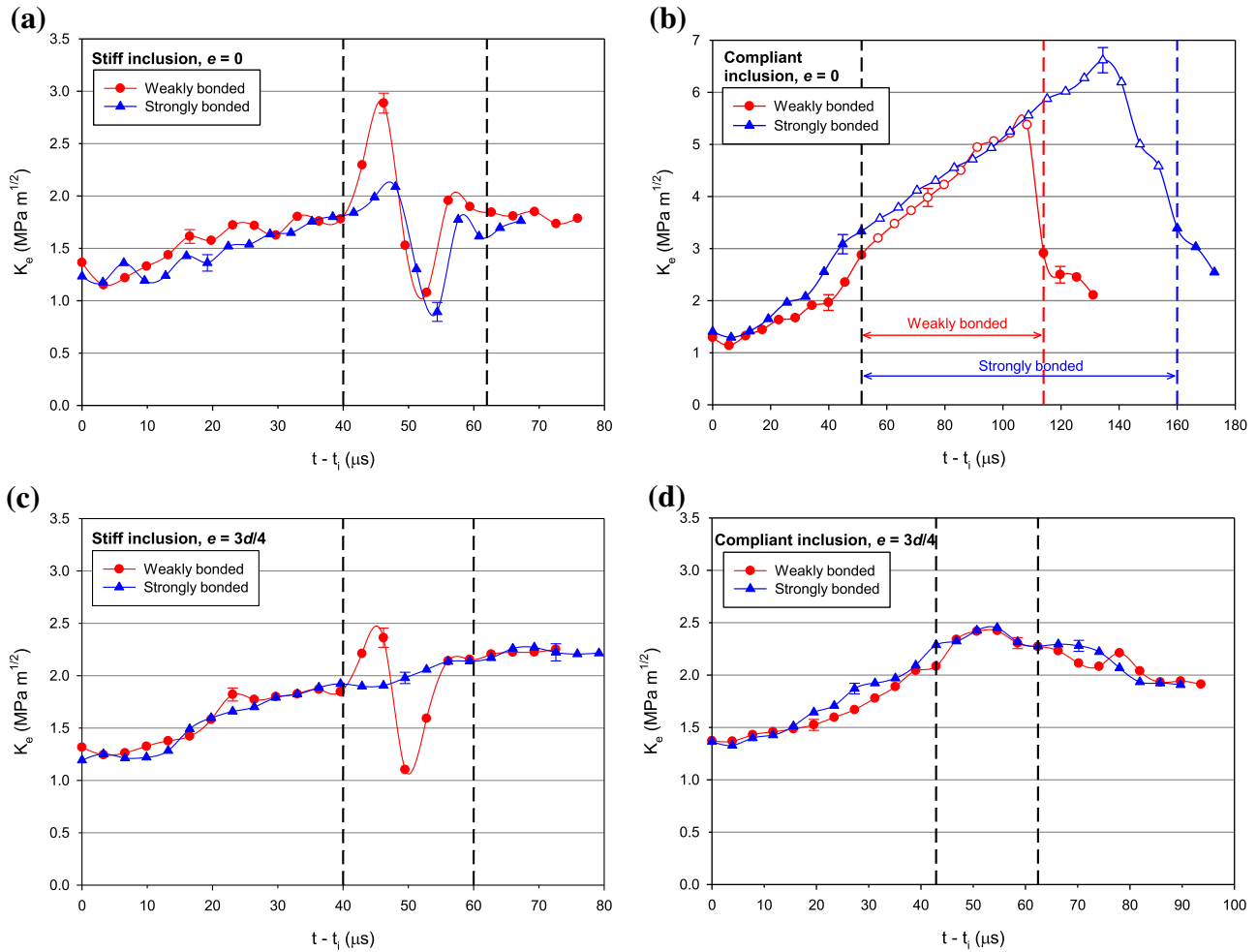
Fig. 9. Crack-tip velocity histories for weakly and strongly bonded inclusion specimens: (a) Stiff inclusion ($e = 0$). (b) Compliant inclusion ($e = 0$). (c) Stiff inclusion ($e = 3d/4$). (d) Compliant inclusion ($e = 3d/4$). The region between vertical broken lines represents crack–inclusion vicinity.

bonded inclusion case compared to the strongly bonded one as the crack overcomes the attraction by the inclusion in the former.

4.4. Stress intensity factor (SIF) histories

The effects of inclusion stiffness and inclusion–matrix adhesion strength on SIFs are presented in Fig. 10. Effective SIF histories for weakly and strongly bonded stiff and compliant inclusion specimens are shown in Fig. 10a and b, respectively, when the inclusion is located symmetrically ($e = 0$). In Fig. 10a for both cases, the effective SIF, K_e at initiation is $\sim$1.3 MPa m$^{1/2}$. After initiation, a slight drop in K_e is evident, and it continues to increase modestly until it reaches a steady state value of $\sim$1.8 MPa m$^{1/2}$. In the crack–inclusion vicinity, for the weakly bonded case, K_e attains a maximum value of $\sim$2.9 MPa m$^{1/2}$ before dropping to $\sim$1.0 MPa m$^{1/2}$ whereas for the strongly bonded counterpart the maximum value of K_e is $\sim$2.1 MPa m$^{1/2}$ before falling to $\sim$0.9 MPa m$^{1/2}$ followed by a steady value of $\sim$1.7 MPa m$^{1/2}$ in both cases after the crack leaves the inclusion vicinity. A steep drop in K_e is quite evident for both weakly and strongly bonded inclusions due to interfacial debonding. This rise and fall in K_e values in the crack–inclusion vicinity is expected due to interfacial crack growth behavior around the stiff-compliant inclusion–matrix interface. Fig. 10b represents effective SIF histories for compliant inclusion specimens at eccentricity $e = 0$. In this case, as observed previously from the crack-tip velocity histories (see Fig. 9b), the crack decelerates as it ap-

proaches the inclusion vicinity and completely stalls at the interface nearly perpendicular to the inclusion for about 60 and 100 μs for weakly and strongly bonded cases, respectively. It should be noted that when the crack front is perpendicular to the inclusion interface, crack-tip singularity is different from the ones described by Eqs. (3)–(7). In this scenario, there is a need for dynamic displacement fields of a crack terminating perpendicular to a bimaterial interface. Due to the current unavailability of dynamic field equations, the K_e values for $e = 0$, have been extracted using those as an approximation for a crack in a homogeneous material ($\varepsilon = 0$ in the Eqs. (3)–(7)). Hence, for the time instants when the crack-tip is nearly perpendicular to the inclusion interface, the K_e values in Fig. 10b are distinguished by open symbols. The K_e at initiation for both specimens is $\sim$1.4 MPa m$^{1/2}$ followed by a modest increase before the crack reaches inclusion proximity. As the crack is arrested at the inclusion, there is a small jump in the K_e followed by a monotonic increase until it reaches a maximum value of $\sim$5.5 and $\sim$6.5 MPa m$^{1/2}$ for weakly and strongly bonded inclusions, respectively. Note that these values are 3–4 times higher than the SIF values during crack initiation in the matrix and is attributed to the crack-tip blunting as the inclusion suffers deformation. When the crack departs the inclusion proximity, K_e drops to $\sim$3.0 MPa m$^{1/2}$ in the weakly bonded case whereas K_e decreases monotonically and reaches $\sim$2.5 MPa m$^{1/2}$ for the strongly bonded inclusion in the observation window.

Fig. 10. Effective stress intensity factor (K_e) histories for weakly and strongly bonded inclusion specimens: (a) Stiff inclusion ($e = 0$). (b) Compliant inclusion ($e = 0$) (note that open symbols represent the approximation of data analysis using homogeneous dynamic crack-tip fields due to the lack of asymptotic descriptions at the moment). (c) Stiff inclusion ($e = 3d/4$). (d) Compliant inclusion ($e = 3d/4$). The region between vertical broken lines represents crack–inclusion vicinity.

Figs. 10c and d depict effective SIF histories for weakly and strongly bonded stiff and compliant inclusion specimens, respectively, for eccentric inclusion cases. As noted in the symmetric cases, K_e at initiation in Fig. 10c is ~1.3 MPa m$^{1/2}$ followed by a slight drop and a monotonic increase until it attains a steady state value of ~1.9 MPa m$^{1/2}$ for both specimens. In the inclusion proximity, for the weakly bonded inclusion case, K_e increases up to ~2.4 MPa m$^{1/2}$ and subsequently drops to ~1.1 MPa m$^{1/2}$ whereas for strongly bonded one this remains unperturbed. The K_e values are nearly equal and overlap on each other as the crack propagates away from the inclusion proximity. For the compliant inclusion cases shown in Fig. 10d, it can be seen that K_e is relatively higher in the strongly bonded case compared to weakly bonded counterpart before the crack interacts with the inclusion followed by nearly similar K_e profiles in the inclusion proximity and beyond.

Note that, the crack-tip singularity (Bogy, 1971; Zak and Williams, 1963) is affected when the crack front is completely stalled at the compliant inclusion interface and the corresponding K_e values represented in Fig. 10b are only estimates. Hence, an *ad-hoc* parameter related to crack-tip opening displacement, $\hat{\delta}_y$ (displacement between crack flanks) was calculated. The quantity $\hat{\delta}_y$ was chosen at a location of $r/B = 0.5$ from the *current* crack-tip position before, during, and after crack–inclusion interaction for weakly and strongly bonded compliant inclusion specimens ($e = 0$). The $\hat{\delta}_y(t)$ histories thus obtained are shown in Fig. 11. It

should be noted that the quantity $\hat{\delta}_y$ is essentially similar to the SIF behavior. It can be seen that $\hat{\delta}_y$ increases monotonically before crack encounters the inclusion and during crack–inclusion interaction when the crack stops at inclusion interface. Following this, $\hat{\delta}_y$ decreases in a monotonic fashion as the crack recedes from the inclusion. Therefore, it is worth noting that the observed trends in $\hat{\delta}_y$ are very much similar to SIF trends shown in Fig. 10b for both weakly and strongly bonded compliant inclusions ($e = 0$).

4.5. Mode-mixity histories

The mode-mixity (ψ) histories are plotted in Fig. 12 for weakly and strongly bonded stiff and compliant inclusion cases ($e = 0$, $3d/4$). In Fig. 12a, following crack initiation, a mildly oscillatory behavior of mode-mixity for about 20 μs can be seen. These oscillations can be attributed to measurement errors and/or transients due to crack initiation. Beyond these initial perturbations, a constant and positive ψ of about 2° is seen before the crack interacts with the inclusion. (Within the data extraction accuracy, this value can be assumed to be zero.) When the crack-tip is in the inclusion vicinity a positive mode-mixity of approximately +42° is seen for the weakly bonded inclusion specimen whereas a negative mode-mixity of about −41° is observed for strongly bonded case. No significance is attached to the sign of mode-mixity as the crack can select paths above or below the inclusion with equal probability.
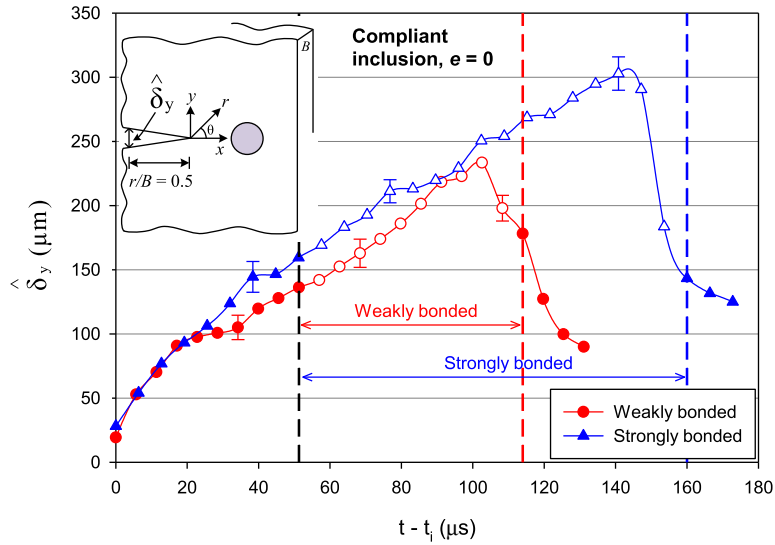
Fig. 11. An *ad-hoc* parameter related to crack-tip opening displacement, $\hat{\delta}_y$ at $r/B = 0.5$ from current crack-tip position for compliant inclusion specimens with $e = 0$. The region between vertical broken lines represents crack–inclusion vicinity.
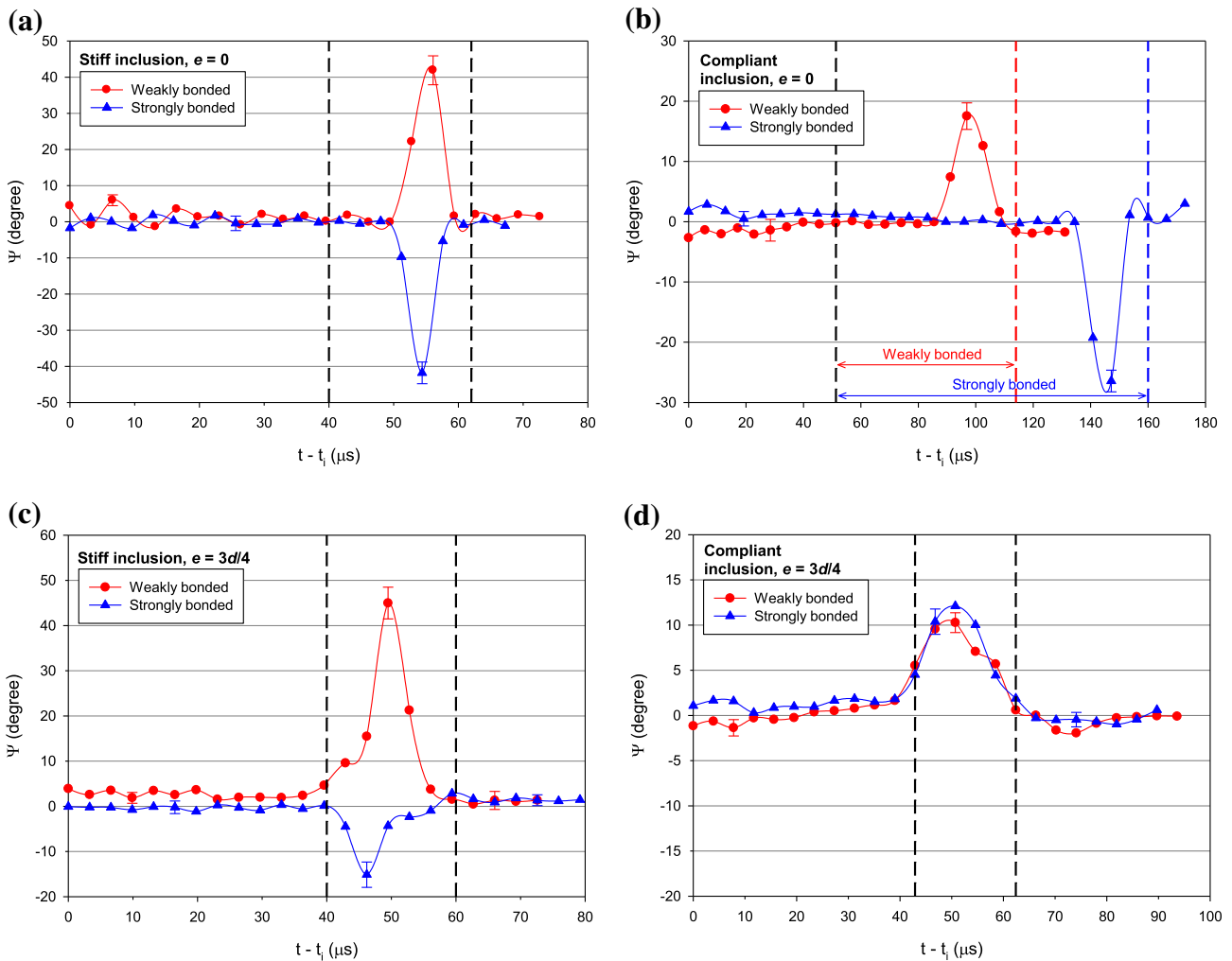
Fig. 12. Mode-mixity (ψ) histories for weakly and strongly bonded inclusion specimens: (a) Stiff inclusion ($e = 0$). (b) Compliant inclusion ($e = 0$). (c) Stiff inclusion ($e = 3d/4$). (d) Compliant inclusion ($e = 3d/4$). The region between vertical broken lines represents crack–inclusion vicinity.

In both cases, after the crack leaves inclusion proximity, ψ attains a constant value of nearly 2°. The mode-mixity histories for

compliant inclusion are shown in Fig. 12b. The weakly bonded inclusion specimen shows a positive mode-mixity of about +18°
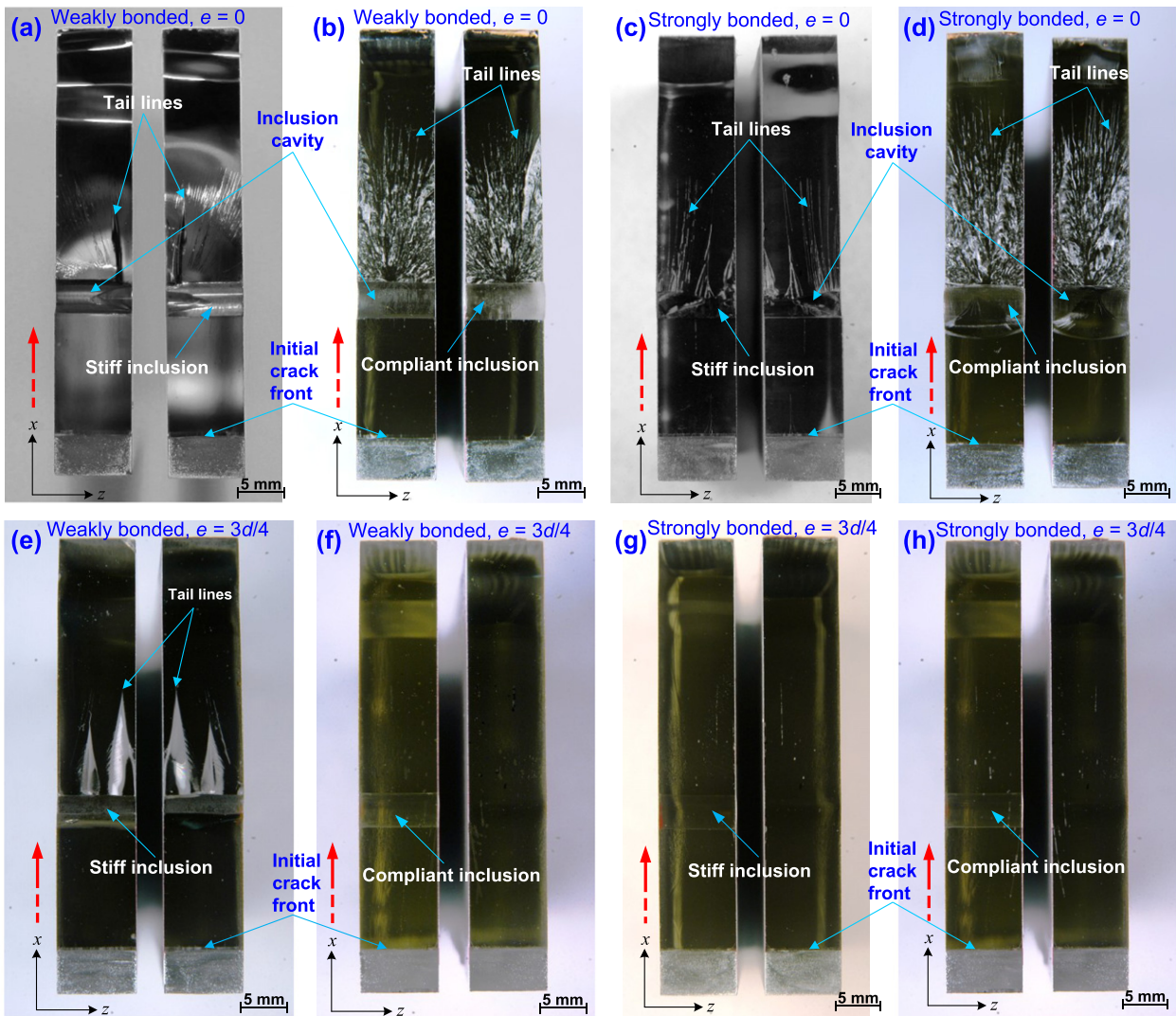
Fig. 13. Macrographs of fractured surfaces (x–z plane) of stiff and compliant inclusion specimens showing fracture surface morphologies: (a) Weakly bonded stiff inclusion ($e = 0$). (b) Weakly bonded compliant inclusion ($e = 0$). (c) Strongly bonded stiff inclusion ($e = 0$). (d) Strongly bonded compliant inclusion ($e = 0$). (e) Weakly bonded stiff inclusion ($e = 3d/4$). (f) Weakly bonded compliant inclusion ($e = 3d/4$). (g) Strongly bonded stiff inclusion ($e = 3d/4$). (h) Strongly bonded compliant inclusion ($e = 3d/4$). The broken arrow indicates crack propagation direction.

Table 2
Material properties of glass and PA6 particles, neat epoxy and particle-filled epoxies.

Material	Density, ρ (kg/m³)	Longitudinal wave speed, C_L (m/s)	Shear wave speed, C_S (m/s)	Elastic modulus, E (GPa)	Poisson's ratio, υ	Tensile strength, σ_{ult} (MPa)	Elongation at break, ε_f (%)
Glass[a] (soda-lime A-glass)	2500	–	–	69	0.190	33	<0.1
PA6[a] (Polyamide-Nylon 6)	1130	–	–	2.3	0.390	78	400
Neat epoxy[b]	1124	2487	1136	3.97	0.368	–	–
Glass-filled epoxy[b] ($V_f = 10\%$)	1279	2627	1257	5.08	0.351	–	–
PA6-filled epoxy[b] ($V_f = 3\%$)	1125	2469	1130	3.93	0.367	–	–

[a] Provided by manufacturer.
[b] In-house measurement (ultrasonic pulse-echo method).

in the inclusion vicinity whereas the strongly bonded counterpart shows a negative mode-mixity of about $-28°$ in the inclusion proximity. The mode-mixity sign changes in these cases are attributed more to the chance associated with the crack path selection.

Figs. 12c and d depict mode-mixity behaviors for stiff and compliant inclusion with eccentricity $e = 3d/4$, respectively. In Fig. 12c, after the initial oscillatory period, the weakly bonded inclusion shows a monotonic increase in ψ as the crack approaches the

inclusion vicinity whereas ψ remains close to zero in the strongly bonded case. Different mode-mixity behaviors can be seen as the crack nears the inclusion for both weakly and strongly bonded inclusion cases. For weakly bonded inclusion specimen, positive mode-mixity values are seen with a maximum of about +45°, indicating a significant attraction of the crack-tip by the weak interface. Contrary to the weakly bonded case, the negative mode-mixity behavior is noticed with a value of −15° suggesting that the crack is repelled by the strong inclusion–matrix interface. In Fig. 12d, it can be seen that the weakly bonded inclusion specimen shows a positive ψ of approximately +10° in the crack–inclusion proximity, whereas positive mode-mixity is evident in the strongly bonded one throughout the fracture event with a maximum ψ of about +13° in the crack–inclusion vicinity. The positive value of ψ in both compliant specimens is expected as the crack is attracted towards the inclusion in both the specimens.

The positive and negative mode-mixity behaviors are consistent with the crack trajectories shown in Fig. 3 for all inclusion eccentricities and bond strengths in stiff and compliant inclusion specimens indicating that the positive and negative mode-mixities signify crack- attraction and crack-repulsion mechanisms. Once the crack leaves the inclusion vicinity, mode-mixities tend to approach zero and crack propagation occurs under dominant mode-I conditions in both stiff and compliant inclusion specimens.

4.6. Fracture surface morphology

The fracture surface morphology often controls the process of dynamic fracture and reveals important clues about the underlying failure mechanisms and the associated energy dissipation characteristics (Arakawa and Takahashi, 1991; Sharon et al., 1996). Accordingly, qualitative fractographic examination was done to further understand the differences in crack growth behavior as a result of stiff and compliant nature of the inclusion, inclusion location and inclusion–matrix adhesion strength. Therefore, the differences in toughening mechanisms in stiff and compliant inclusions embedded in an epoxy matrix are explained by examining fracture surfaces as shown in Fig. 13. The photographs of the entire x–z plane of dynamically fractured weakly and strongly bonded stiff and compliant inclusion specimens with eccentricities, $e = 0$ and $3d/4$ are shown in Fig. 13a–h with both ligaments of the fractured specimens, one ligament showing the inclusion cavity and the other showing the inclusion. The broken arrow indicates the direction of crack propagation. It can be seen that in all these macrographs, the fracture surfaces just before the crack reaches the inclusion are relatively smooth and shiny when compared to the region after it grows past the stiff and compliant inclusions, indicating brittle fracture.

Figs. 13a, b and c, d depict fracture surface morphology of weakly and strongly bonded stiff and compliant inclusion specimens ($e = 0$), respectively. In the weakly and strongly bonded stiff inclusion specimens (see Fig. 13a and c), fracture surfaces after crack–inclusion interaction consist of tails lines and river lines with high frequency tail lines in the former compared to the latter. In the compliant inclusion counterparts (see Fig. 13b and d), much higher surface roughness and ruggedness is clearly evident in both weakly and strongly bonded cases with high frequency of tail lines, larger and intensely rough region in the latter compared to the former. Further, it can be seen that the compliant inclusion in the strongly bonded case (see Fig. 13d) is surrounded by a pool (or pocket) of epoxy showing a strong inclusion–matrix bonding and clearly demonstrates that the roughening of compliant inclusion produced a strong inclusion–matrix interface (as discussed in the sample preparation section). It is interesting to note that this epoxy residue is maximum just before the crack encounters the inclusion. As the crack advances, the epoxy residue diminishes (tapers off) at

the other end symmetrically with respect to the center of crack front. The fracture surfaces of both ligaments in case of the compliant inclusion (see Fig. 13b and d) reveal that a highly transient fracture has occurred after the crack front leaves the inclusion, showing very rough, highly textured, surfaces containing a large number of tail lines and deep furrows. Also, the fracture surface morphologies in Fig. 13b and d give an indication of hackle regions (Lampman, 2003) which are generally associated with violent fracture in which tremendous amount of fracture energy is absorbed through both plastic deformation and by generation of additional fracture surface areas. Moreover, as crack propagates, the elastic
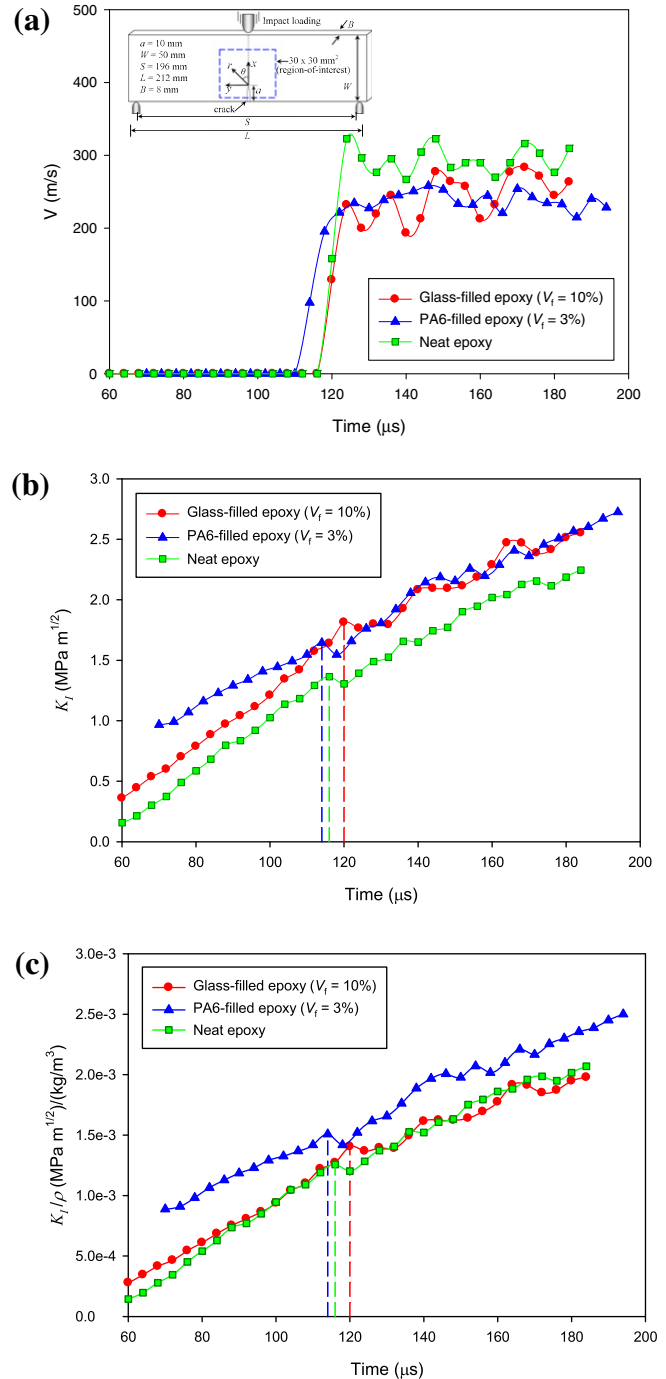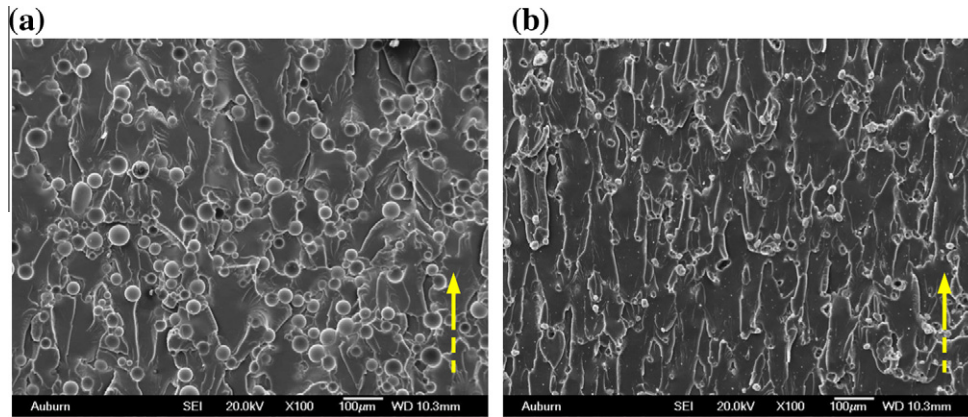

Fig. 14. Dynamic fracture of glass-filled and PA6-filled epoxies: (a) Crack-tip velocity histories (inset shows specimen geometry and loading configuration). (b) Mode-I SIF histories. (c) Mode-I *specific* SIF (KI/ρ) histories.

Fig. 15. SEM micrographs of fractured surfaces (x–z plane): (a) Glass-filled epoxy ($V_f = 10\%$). (b) PA6-filled epoxy ($V_f = 3\%$). The broken arrow indicates crack propagation direction.
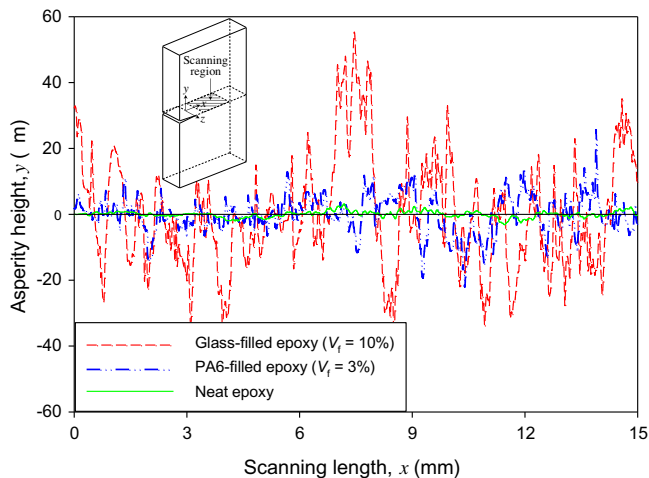
Fig. 16. Fracture surface profiles for glass-filled, PA6-filled and neat epoxy specimens (inset shows schematic representation of crack growth and scanning region selected for roughness measurement (x–z plane)).

strain energy is released and as the crack driving force increases along with sufficiently high crack velocity, a single crack front begins to branch into many smaller (micro) crack fronts, increasing energy dissipation by creating new fracture surfaces. On the other hand, the stiff inclusion specimen ligaments indicate much lower roughness, fewer tail lines and river line morphology. The presence of high concentration of tail lines and higher surface ruggedness in case of compliant inclusion specimens suggest greater energy dissipation and accounts for improved fracture toughness compared to the stiff inclusion specimens.

Figs. 13e, f and g, h depict fracture surface morphology of weakly and strongly bonded stiff and compliant inclusion specimens ($e = 3d/4$), respectively. In Fig. 13e, as the crack leaves the stiff inclusion, wider pockets of epoxy at the interface are visible. Subsequently these pockets converge into tail lines with further crack propagation, whereas in the case of compliant inclusion no such features are present (Fig. 13f). In the strongly bonded counterparts as shown in Fig. 13f–h both stiff and compliant inclusion specimens, fracture surfaces are smooth and shiny and macroscopically do not reveal any significant information.

5. Discussion

The experimental results demonstrate the underlying physics of fast fracture when a matrix crack encounters an inhomogeneity in or near its path. The results also emphasize the importance of inclusion stiffness, inclusion–matrix interfacial strength and inclusion eccentricity affecting the fracture parameters and energy dissipation characteristics resulting in different crack trajectories. Interestingly, unlike the stiff inclusion case, compliant inclusion attracted the propagating crack in all cases regardless of the inclusion–matrix adhesion strength (see Fig. 3f and h). The crack velocity rapidly increased (~85% of the Rayleigh wave speed in neat epoxy) during the interaction with symmetrically located and weakly bonded stiff or compliant inclusions as the matrix crack became an interfacial crack before getting trapped. The crack growth behavior in case of compliant inclusions further suggests that a growing crack could be arrested for relatively long duration of time. That is, failure could be resisted with the aid of compliant fillers by forcing the growing crack to encounter obstacles. The inclusion stiffness also affected the stress wave loading of the crack-tip as seen by the peak impact force (compressive) recorded by the tup in Fig. 7a–d. In the stiff inclusion specimens the recorded force was higher than the compliant counterpart since the reflected stress waves from the stiff inclusion reflected back as compressive waves whereas the same reflected back as tensile waves in the compliant inclusion cases. In terms of crack tip parameters, the weakly bonded stiff inclusions resulted in higher dynamic SIF values than the strongly bonded ones in the crack–inclusion vicinity. This observation is consistent with the results of Kitey and Tippur (2005a) on dynamic fracture behavior of micron size glass-filled epoxy. Further, a strongly bonded compliant inclusion improved the overall fracture toughness more than its weakly bonded counterpart as localized ductility of the inclusion was fully exploited in the former case. The compliant inclusion configurations showed significantly higher crack growth resistance than the stiff inclusion cases, a 3–4 fold increase in dynamic SIF.

6. Implications to dynamic fracture of particle filled-epoxies

The present study on dynamic crack growth past stiff and compliant inclusions has real life applications involving particulate reinforced polymer composites. In general, the small volume fractions (V_f) of filler (stiff/brittle or compliant/ductile) particles in polymeric materials are used to enhance overall strength, impact energy absorption and thermo-mechanical characteristics of the resulting composite system. Hence, in the context of crack–inclusion interaction studies presented here, the dynamic fracture of particle filled-epoxies was also carried out in order to characterize the dynamic fracture behavior.

Two types of micron size fillers were used, one is soda-lime glass (A-glass) particles of average diameter 35 μm (Spheriglass-3000, Potters Industries Inc., USA), and the other is PA6 (Polyamide-Nylon 6) of mean particle size 20 μm (Goodfellow Cambridge Ltd., UK). The latter is used as the ductile filler due to the lack of commercial availability of micron size polyurethane filler. Each type of filler was uniformly dispersed in the same low viscosity epoxy used in the earlier part of the study. Note that both kinds of particles were weakly bonded to the matrix and three types of specimens were prepared, namely glass-filled epoxy (V_f = 10%), PA6-filled epoxy (V_f = 3%), and neat epoxy. The physical and elastic properties of glass and PA6 fillers, and resultant filled-epoxies are shown in Table 2. Evidently PA6 is relatively compliant relative to neat epoxy and highly ductile with a failure strain (ε_f) of ~400% when compared to glass (ε_f < 0.1%). The dynamic fracture tests on glass and PA6 filled-epoxies were conducted to quantify crack-tip deformations and hence crack growth parameters using the experimental methodology described earlier.

Fig. 14 shows the comparison of dynamic fracture results of the filled-epoxies relative to the neat epoxy. The crack velocity histories are shown in Fig. 14a along with an inset depicting specimen geometry and loading configuration. It can be seen that in filled-epoxies, the crack initiated later and subsequently propagated at a lower speed than in the neat epoxy. Following crack initiation, PA6-filled epoxy had nearly steady crack growth relative to the one seen in neat as well as glass-filled epoxy. The mode-I SIF (K_I) and the *specific* SIF (K_I/ρ) histories for each specimen are shown in Fig. 14b and c, respectively. The vertical broken lines corresponding to each experiment indicate the time at which crack initiated after the initial impact. From Fig. 14b, it can be seen that both glass and PA6 filled-epoxies show higher K_I values in the

pre- as well as post-initiation regimes when compared to neat epoxy. It is interesting to note that less than a third of PA6 (V_f = 3%) produces the same post-initiation K_I response as the one due to 10% V_f glass. Further, from Fig. 14c it is noteworthy that PA6 results in increased *specific* SIF (K_I/ρ) (~30% higher) throughout the fracture event when compared to both glass-filled and neat epoxy specimens.

In order to characterize fracture surface morphology, scanning electron microscopy was performed. Figs. 15a and b show SEM micrographs of fractured surfaces (*x–z* plane) of glass-filled and PA6-filled epoxies, respectively. The broken arrow in these micrographs indicates crack propagation direction. The microscopic examination of glass-filled epoxy in Fig. 15a reveals particle–matrix debonding which results in crack front trapping. Also, zigzag micro-crack patterns along the crack growth direction and river lines can be clearly seen. The micrograph in Fig. 15b shows tail lines and matrix flow parabolas in the direction of crack propagation. Moreover, PA6 particles seem to have undergone nonlinear deformations due their high ductility. To further understand fracture surface morphology, quantitative micro-measurements were also performed using a Dektak-150 stylus profiler with a stylus of root radius of 2 μm. Fig. 16 shows fractured surface profiles for filled-composites and neat epoxy with an inset depicting crack growth and scanning region (*x–z* plane) for roughness measurements. The surface profile of glass-filled epoxy shows longer wavelengths and larger amplitudes relative to PA6-filled epoxy. The neat epoxy, on the other hand, shows least surface amplitude with surface profile very close to the mean surface. The fracture-induced surface roughness (after discounting the roughness due to filler particles or their foot prints themselves; see Kitey and Tippur, 2005b) was evaluated and found to be approximately 10.6 μm
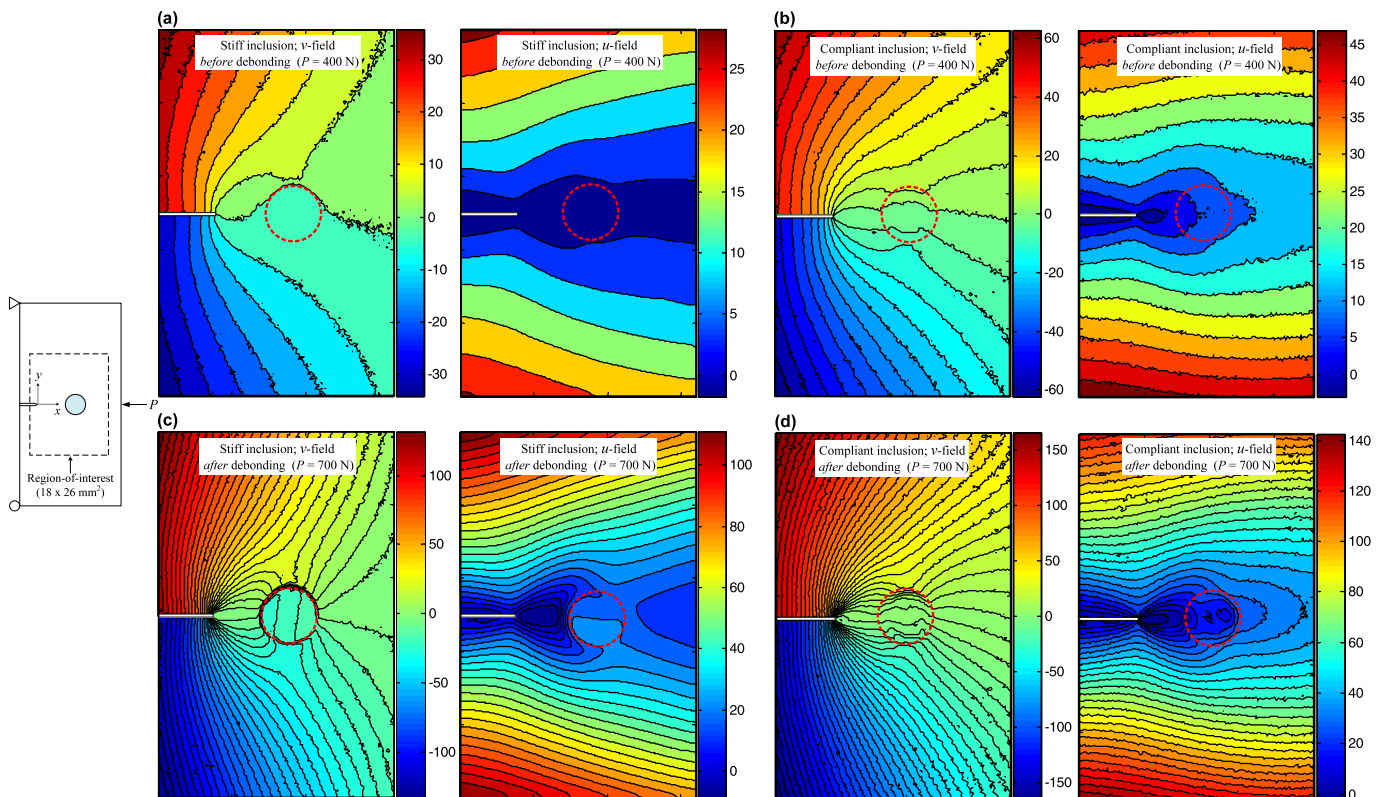
Fig. 17. Crack-opening (*v*-field) and crack-sliding (*u*-field) displacement contours from quasi-static fracture tests for strongly bonded stiff and compliant inclusion specimens at eccentricity, *e* = 0 (contour interval: 5 μm). Color-bars indicate displacements in μm. The location of cylindrical inclusion is represented by dotted circle. (a) Stiff inclusion, *before* debonding at *P* = 400 N, (b) Compliant inclusion, *before* debonding at *P* = 400 N, (c) Stiff inclusion, *after* debonding at *P* = 700 N, (d) Compliant inclusion, *after* debonding at *P* = 700 N. (For interpretation of the references to color in this figure, the reader is referred to the web version of this article.)

and 3.8 μm for glass-filled and PA6-filled epoxies, respectively. Considering a threefold lower volume fraction of PA6 filler in epoxy, the fracture-induced roughness is higher in case of PA6. Furthermore, energy dissipation within the PA6 particles during crack–inclusion interaction has also contributes to this improved performance relative to glass-filled epoxy.

7. Conclusions

The role of inclusion stiffness (and elastic impedance) mismatch and interfacial strength on dynamic matrix crack growth past an embedded inclusion was studied experimentally. Two different mismatches – stiff and compliant – and adhesion strengths – weak and strong – were investigated for symmetric and eccentric crack growth configurations. Experimental simulations were carried out under stress wave dominant loading conditions on epoxy samples embedded with glass and polyurethane inclusions. In-plane crack-tip deformations were measured in real time optically before, during and after crack–inclusion interactions. Fractured specimens show different crack trajectories and crack velocities for each inclusion location and inclusion–matrix bond strengths. For weakly bonded inclusion specimens, higher crack velocities were observed for both stiff as well as compliant inclusions when compared to the strongly bonded ones. The crack was completely stalled for about a third to half of the duration needed to complete the fracture of samples in the case of compliant inclusion samples. The dynamically propagating crack was attracted and arrested by the weak inclusion interface for both symmetric glass and polyurethane inclusion cases whereas it was deflected away by the stronger one for glass and attracted by polyurethane inclusion when situated eccentrically. The inclusion elastic moduli and inclusion–matrix interfacial strength also affected the effective SIF, K_e. The mode-mixity histories capture the physical crack growth observations. The compliant inclusion specimens showed much higher fracture toughness for weak and strong bond strengths when compared to the glass inclusion counterparts. The macroscopic observation of dynamically fractured specimens accounted for greater crack resistance in compliant inclusion specimens compared to the stiff inclusion ones.

The broader implications of crack–inclusion interaction scenarios were tested by conducting limited dynamic fracture experiments on glass- and PA6-particle filled epoxies. The results showed that 3% volume fraction of PA6 in epoxy produced the same fracture toughness enhancement as 10% volume fraction of
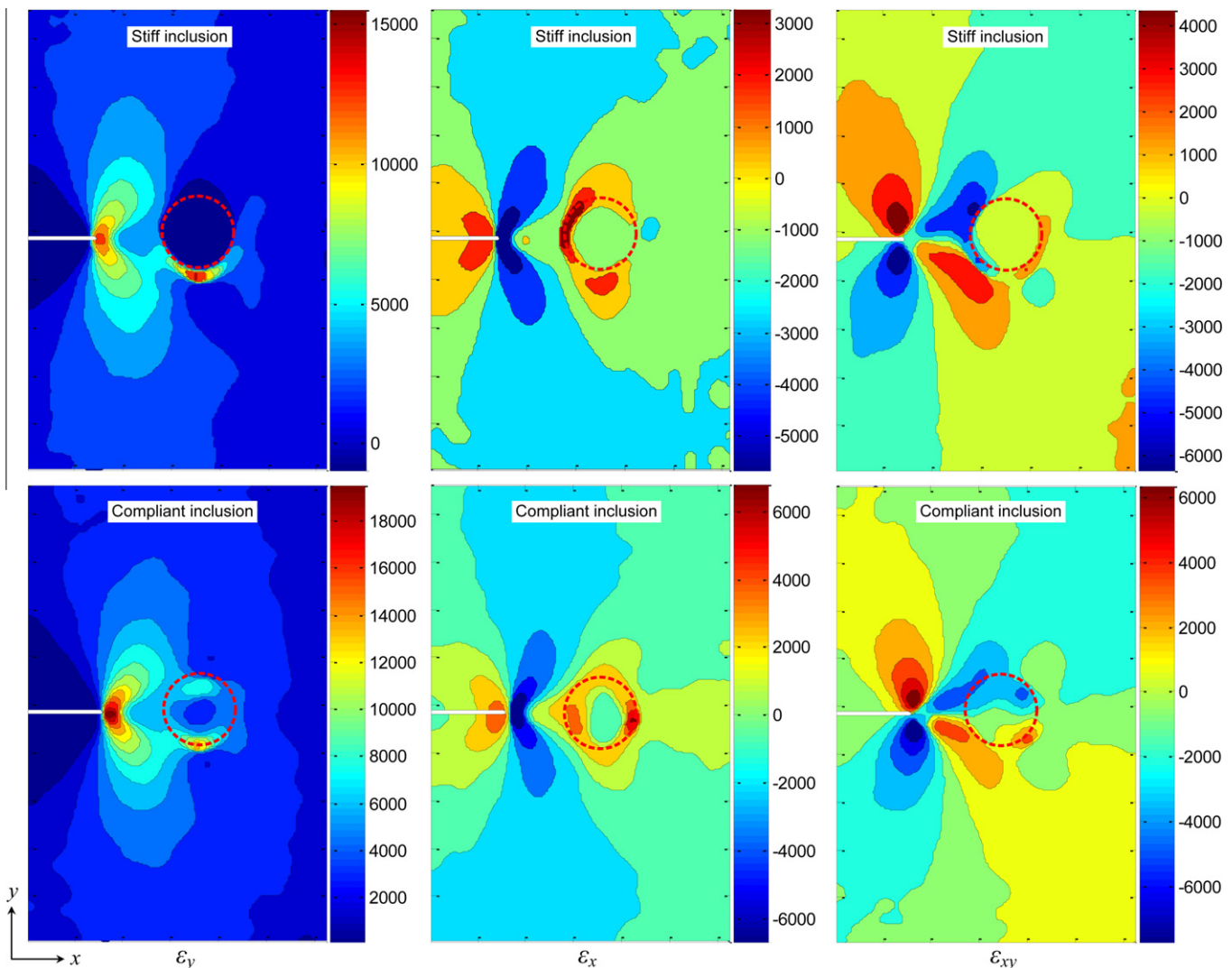
Fig. 18. Crack-tip normal strains (ε_y, ε_x in $\mu\varepsilon$) and shear strains (ε_{xy} in $\mu\varepsilon$) from quasi-static fracture tests for strongly bonded stiff and compliant inclusion specimens *after* debonding at eccentricity, $e = 0$ and, at a load level, $P = 700$ N. (Contour interval: $1500\mu\varepsilon$). Color-bars indicate strains in $\mu\varepsilon$. The location of cylindrical inclusion is shown by dotted circle. (For interpretation of the references to color in this legend, the reader is referred to the web version of this article.)

glass when both fillers are weakly bonded to the matrix. The former did not reduce the stiffness of the resulting composite when compared to neat epoxy yet produced approximately 30% higher *specific* dynamic fracture toughness relative to both neat and glass-filled epoxy.

Acknowledgements

Appendix A. Quasi-static crack–inclusion interaction

The crack–inclusion interaction was studied statically in greater detail (higher spatial and grayscale resolutions). A digital SLR camera with 2000×3008 pixel resolution and 10 bit (0–1023) grayscale digitization was used to capture details within the inclusion and in the inclusion vicinity. A few selected crack-opening (v-field) and crack-sliding (u-field) displacement contours for a symmetrically located ($e = 0$) strongly bonded stiff and compliant inclusion specimens are shown in Fig. 17 *before* and *after* debonding of the inclusion. Figs. 17a and b show displacement contours depicting crack–inclusion interaction *before* debonding and Figs. 17c and d show the same *after* debonding for stiff and compliant inclusion specimens. From Fig. 17a–d it can be seen that the contours are symmetric near the crack-tip, indicating dominant mode-I conditions and contours around the inclusion discontinuous after debonding occurs. After debonding, the contour lines within the stiff inclusion in Fig. 17c are parallel to each other and equally spaced showing rigid rotation of the inclusion relative to the matrix. This is similar to the observation made by Savalia and Tippur (2007) using moiré interferometry. On the other hand, for the compliant inclusion, the non-uniform deformations within the inclusion can be clearly seen in Fig. 17b and d, suggesting substantial straining of the inclusion. The contours are denser near the top/bottom edges of the inclusion in Fig. 17d is indicative of large strains compared to the mid-portion of the inclusion.

The measured crack-tip normal strains ($\varepsilon_y, \varepsilon_x$) and shear strains ($\varepsilon_{xy}$) for symmetrically located ($e = 0$) strongly bonded stiff and compliant inclusion specimens are shown in Fig. 18 *after* the inclusion debonds from the matrix. The concentration and symmetry of ε_y, ε_x, and ε_{xy} contours around the crack-tip can be seen in these figures. A high strain concentration in ε_y field is quite evident for both stiff and compliant inclusion specimens in the debonding region. As expected, a nearly zero ε_y strain can be seen over the stiff inclusion, whereas the contours ranging from ~2000 to ~7000 microstrains are quite evident within the compliant inclusion with least strain at the center of the inclusion. The redistribution of strains can also be seen ahead of the crack-tip and in the inclusion vicinity when the inclusion debonds from the matrix. In the case of ε_x strains, the contours within the compliant inclusion are compressed and elongated in the x and y- directions, respectively, due to straining of the inclusion whereas no such features are evident in the case of stiff inclusion. Further, ε_x strains are tensile and concentrated on the opposite ends of the inclusion in the stiff and compliant cases. The ε_{xy} strains show skew symmetry in strain contours around the crack-tip and in the inclusion vicinity. The ε_{xy} contours are tangential around the inclusion in both stiff and compliant inclusions with nearly zero shear strain within the stiff

case and a relatively large shear deformation in the compliant counterpart.

References

Arakawa, K., Takahashi, K., 1991. Relationships between fracture parameters and fracture surface roughness of brittle polymers. International Journal of Fracture 48, 103–114.

Atkinson, C., 1972. Interaction between a crack and inclusion. International Journal of Engineering Science 10, 127–136.

Bogy, D.B., 1971. On the plane elastostatic problem of a loaded crack terminating at a material interface. Journal of Applied Mechanics 38, 911–918.

Bourne, N.K., Millett, J.C.F., Field, J.E., 1999. On the strength of shocked glasses. Proceedings of Royal Society of London A 455, 1275–1282.

Bush, M.B., 1998. The interaction between a crack and a particle cluster. International Journal of Fracture 88, 215–232.

Cheeseman, B.A., Santare, M.H., 2000. The interaction of a curved crack with a circular elastic inclusion. International Journal of Fracture 103, 259–277.

Deng, X., 1993. General crack-tip fields for stationary and steadily growing interface cracks in anisotropic bimaterials. Journal of Applied Mechanics 60, 183–189.

Erdogan, F., Gupta, G.D., Ratwani, M., 1974. Interaction between a circular inclusion and an arbitrarily oriented crack. Journal of Applied Mechanics – Transactions of ASME 41, 1007–1013.

Eroshkin, O., Tsukrov, I., 2005. On micromechanical modeling of particulate composites with inclusions of various shapes. International Journal of Solids and Structures 42, 409–427.

Geisler, B., Kelley, F.N., 1994. Rubbery and rigid particle toughening of epoxy resins. Journal of Applied Polymer Science 54, 177–189.

Hussain, M., Nakahira, A., Nishijima, S., Niihara, K., 1996. Fracture behavior and fracture toughness of particulate filled epoxy composites. Materials Letters 27, 21–25.

Jajam, K.C., Tippur, H.V., 2011. An experimental investigation of dynamic crack growth past a stiff inclusion. Engineering Fracture Mechanics 78, 1289–1305.

Kinloch, A.J., Shaw, S.J., Tod, D.A., Hunston, D.L., 1983a. Deformation and fracture behavior of a rubber-toughened epoxy: 1. Microstructure and fracture studies. Polymer 24, 1341–1354.

Kinloch, A.J., Shaw, S.J., Hunston, D.L., 1983b. Deformation and fracture behaviour of a rubber-toughened epoxy: 2. Failure criteria. Polymer 24, 1355–1363.

Kinloch, A.J., Yuen, M.L., Jenkins, S.D., 1994. Thermoplastic-toughened epoxy polymers. Journal of Materials Science 29, 3781–3790.

Kirugulige, M.S., Tippur, H.V., 2009. Measurement of fracture parameters for a mixed-mode crack driven by stress waves using image correlation technique and high-speed digital photography. Strain 45, 108–122.

Kirugulige, M.S., Tippur, H.V., Denney, T.S., 2007. Measurement of transient deformations using digital image correlation method and high-speed photography: application to dynamic fracture. Applied Optics 46, 5083–5096.

Kitey, R., Phan, A.V., Tippur, H.V., Kaplan, T., 2006. Modeling of crack growth through particulate clusters in brittle matrix by symmetric-Galerkin boundary element method. International Journal of Fracture 141, 11–25.

Kitey, R., Tippur, H.V., 2005a. Role of particle size and filler-matrix adhesion on dynamic fracture of glass-filled epoxy: I. Macromeasurements. Acta Materialia 53, 1153–1165.

Kitey, R., Tippur, H.V., 2005b. Role of particle size and filler-matrix adhesion on dynamic fracture of glass-filled epoxy: II. Linkage between macro- and micro-measurements. Acta Materialia 53, 1167–1178.

Kitey, R., Tippur, H.V., 2008. Dynamic crack growth past a stiff inclusion: optical investigation of inclusion eccentricity and inclusion–matrix adhesion strength. Experimental Mechanics 48, 37–53.

Kushch, V.I., Shmegera, S.V., Mishnaevsky Jr, L., 2010. Elastic interaction of partially debonded circular inclusions. I: Theoretical solution. International Journal of Solids and Structures 47, 1961–1971.

Lampman, S., 2003. Characterization and Failure Analysis of Plastics, first ed. ASM International, Ohio.

Lee, D., Tippur, H., Kirugulige, M., Bogert, P., 2009. Experimental study of dynamic crack growth in unidirectional graphite/epoxy composites using digital image correlation method and high-speed photography. Journal of Composite Materials 43, 2081–2108.

Mantic, V., 2009. Interface crack onset at a circular cylindrical inclusion under a remote transverse tension. Application of a coupled stress and energy criterion. International Journal of Solids and Structures 46, 1287–1304.

Mogilevskaya, S.G., Crouch, S.L., 2002. A Galerkin boundary integral method for multiple circular elastic inclusions with homogeneously imperfect interfaces. International Journal of Solids and Structures 39, 4723–4746.

Mogilevskaya, S.G., Crouch, S.L., 2004. A Galerkin boundary integral method for multiple circular elastic inclusions with uniform interphase layers. International Journal of Solids and Structures 41, 1285–1311.

O'Toole, B.J., Santare, M.H., 1990. Photoelastic investigation of crack–inclusion interaction. Experimental Mechanics 30, 253–257.

Savalia, P.C., Tippur, H.V., 2007. A study of crack–inclusion interactions and matrix–inclusion debonding using Moiré interferometry and finite element method. Experimental Mechanics 47, 533–547.

Savalia, P.C., Tippur, H.V., Kirugulige, M.S., 2008. A numerical study of inclusion–matrix debonding in the presence of a nearby crack. Engineering Fracture Mechanics 75, 926–942.

Sharon, E., Gross, S.P., Fineberg, J., 1996. Energy Dissipation in Dynamic Fracture. Physical Review Letters 76, 2117.

Tamate, O., 1968. The effect of a circular inclusion on the stresses around a line crack in a sheet under tension. International Journal of Fracture 4, 257–266.

Tippur, H.V., Krishnaswamy, S., Rosakis, A.J., 1991. Optical mapping of crack tip deformations using the methods of transmission and reflection coherent gradient sensing: a study of crack tip K-dominance. International Journal of Fracture 52, 91–117.

Tirosh, J., Nachlis, W., Hunston, D., 1995. Strength behavior of toughened polymers by fibrous (or particulate) elastomers. Mechanics of Materials 19, 329–342.

Zak, A.R., Williams, M.L., 1963. Crack point stress singularities at a bimaterial interface. Journal of Applied Mechanics 30, 142–143.